



**Politecnico
di Torino**

Politecnico di Torino

Department of Applied Science and Technology

Nanotechnologies for ICTs

Synthesis and characterization of bismuth oxide based and c-dots hybrid materials for teragnostic applications

Master thesis project of:

Solomiya Pidkova

277968

Supervisor:

Prof. Alberto Tagliaferro

October 2021

Contents

1	Introduction	5
1.1	Teragnostics	5
1.2	C-Dots	7
1.2.1	C-Dots properties and characteristics	8
1.2.2	C-Dots preparation	13
1.2.3	Bismuth Oxide properties and applications	15
1.2.4	Bismuth Oxide micro and nano particles preparation	17
2	Materials and Methods	19
2.1	Materials	19
2.2	Synthesis of C-Dots	20
2.2.1	Thermal treatment and purification by centrifugation	20
2.2.2	Purification by dialysis	21
2.3	Synthesis of Bismuth Oxide base microparticles	23
2.3.1	Hydrothermal synthesis	23
2.3.2	Solid state synthesis	24
2.4	Synthesis of Bismuth Oxide and C-Dots conjugations	25
2.4.1	Solid state Bismuth Oxide based particles with different types of C-Dots	25
2.4.2	Hydrothermally prepared Bismuth Oxide microparticles with different types of C-Dots	25
2.4.3	Direct synthesis of Bismuth Oxide microparticles and conjugation with C-Dots	26
3	Results and Discussions	28
3.1	C-Dots	28
3.1.1	FT-IR spectroscopy	30
3.1.2	Raman spectroscopy	35
3.1.3	Absorbance UV/VIS	37
3.1.4	Fluorometer analysis	38
3.2	Bismuth Oxide based microparticles	41
3.2.1	FESEM	44
3.2.2	Raman spectroscopy	51
3.3	Conjugations	53
3.3.1	FESEM	53

3.3.2	FT-IR spectroscopy	56
3.3.3	Raman spectroscopy	60
3.3.4	Absorbance UV/VIS	64
3.3.5	Fluorometer analisys	66
4	Conclusions	67
5	Acknowledgements	71
6	Bibliography	73

Abstract

In the last years nanotechnology applied to the medical field arouses a lot of interest. In this thesis work carbon dots (C-Dots) and microparticles of Bismuth Oxide synthesized and subsequently conjugated. C-Dots are composed by sp^2 and sp^3 hybridized carbon structures with size of few nanometers. Since their discovery, C-Dots have attracted a great attention due to their simple synthesis, solubility, photoluminescence, biocompatibility and presence of surface functional groups acting as anchoring points for a variety of drugs. The bottom-up approach has been used for the C-Dots synthesis through citric acid (CA) and p-Phenylendiamine (DPA), in order to promote polymerization, and subsequent purification by means of two different methods. The first one includes carbonization by thermal treatment at different temperatures (250°C, 350°C and 450°C were tested) and centrifugation. The second purification process is performed by dialysis, which exploits the difference in osmosis pressure phenomenon. It can be hypothesized that in both cases the C-Dots with random cross-linked polymeric structures which are organized in parallel planes with external functional groups are obtained. Comparing two results with IR spectroscopy it arise that the heat treatment produces more heterogeneous and functionalizable structure. The dialyzed one has more compact, less flexible so more aromatic structure. The C-Dots synthesis has been repeated adding polyethyleneglycol (PEG-4000) as a reagent. PEG acts as a separator which avoids the C-Dots aggregation, favors the aromatic compounds condensation and reacting with its functional groups maximizes the subsequent conjugation. Bi_2O_3 microparticles, thanks to their radiopacity, are applicable in the teragnostic and diagnostic purposes. They are insoluble, but it is possible to bring them in suspension in water by surrounding them with C-Dots. These particles can cause inflammatory phenomena, oxidative stress and cytotoxicity in some cells, so they must be big enough to not cross the cell membrane, but at the same time, small enough to remain suspended by C-Dots. Bismuth Oxide microparticles has been prepared by hydrothermal synthesis with active surfactant that direct their growth and by solid state synthesis without solvent at different calcinations temperatures to promote the thermal decomposition. The conjugation has been performed by mixing the solid state synthesized particles with different types of purified C-Dots and subsequently centrifuging the product in order to separate the soluble part and residue, which contains the Bismuth Oxide microparticles conjugated with C-Dots through the weak surface interactions of $\pi - d$ type. Also the direct synthesis of microparticles and their conjugation with C-Dots has been performed with a satisfying result by repeating all steps of the hydrothermal synthesis and adding C-Dots in the solution.

The aim of this thesis project is synthesis and the conjugation of the Carbon Dots (C-Dots) with Bismuth Oxide microparticles. Bismuth Oxide particles, due to their radiopacity, could be implemented in teragnostic purposes. However, they are insoluble and must be conjugated on the surface with C-Dots, which present an excellent solubility and bring them into suspension in the water. It

is important producing Bismuth Oxide particle quite small to remain suspended when surrounded by C-Dots, which are biocompatible and can transport drugs connected to their surface functional groups. Bismuth oxide particles must also be big enough to not cross a cell barrier. This could cause inflammatory phenomena, oxidative stress and cytotoxicity. Due to the fact that C-Dots and Bismuth Oxide particles interact only on their surfaces, makes possible teragnostic inside the cell barrier through C-Dots, which can cross its membrane, and outside it through Bismuth Oxide particles which can't cross a cell membrane.

CHAPTER 1

Introduction

1.1 Teragnostics

In the last years, Nanotechnology have gained importance and becomes one of the most exiting vanguard field. Nanotechnology regards design, production, characterization and applications of structures, devices and systems by controlling their shape and size at the nanometric scale. Engineering, Biology, Medicine, Chemistry, Physics and many other scientific and technological fields take advantage from Nanotechnology[1].

The advantage of applying Nanotechnology to medicine arises from the possibility to interact with the bodies at subcellular (i.e. molecular) level with a high efficiency and specificity. Considering this, modern diagnostic techniques is to combine the diagnostic imaging capabilities with nanostructural therapeutic interventions in order to obtain teragnostic platforms, as schematically represented in figure 1.1 [2,3,4].

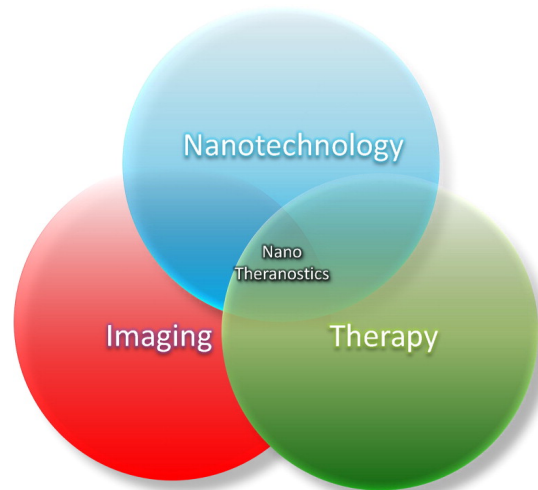


Figure 1.1: Theragnostic aspects: nanotechnology, diagnostic and therapy.

One of the most interesting and promising applications of the teragnostic concerns oncology treatments. Nowadays, 50% of oncological patients are submitted to the radiation therapy [5]. This technique involves high energy X-rays that hit tumour tissues causing free radical or DNA damage. In radiotherapy the side effects are proportional to the tumour mass radiation resistance, which usually is relatively high. Poor discrimination between cancer and healthy cells and inaccuracy of tumour mass localization cause too large side effects. Recent success of the nanotechnology develops a new family of nanomaterials employed in cancer detection, in vivo imaging, drug delivery and others. These exploit the increase of photon absorption due to the high atomic number in order to improve radiosensitizing. The use of nanoparticles it is possible to enhance a localized therapeutic intervention favouring the tumour radiosensitivity, minimize side effects due to the localized treatment and use imaging properties for a real time monitoring. A lot of studies have shown that micro and nanoparticles selective delivery of therapeutic substances into a tumour tissue improves the bioavailability of cytotoxic agents and reduces toxic effects to healthy tissues. Therapeutic nanoparticles were produced from silver, gold and gadolinium, but recently, also Bismuth Oxide (Bi_2O_3) nanoparticles were implemented for these purpose [6]. In following section Bismuth Oxide nanoparticles teragnostic features will be analyzed in detail.

Also C-Dots, carbon based nanoparticles, seems to be promising for the teragnostic applications. They are soluble, biocompatible, non toxic nanoparticles and due to their surface functionalization can perform drug delivery [7]. Photoluminescence (PL) arising from the functional groups can implement also imaging behaviour simultaneously. Thermo dependent PL can be implemented for the release of drugs at body temperature [8].

1.2 C-Dots

C-Dots are the newest member of the carbon nanoscale materials, they were accidentally discovered in arc discharged soot in 2004, during the electrophoretic analysis and purification of Single-Walled Carbon Nanotubes (SWCNTs) performed by Xu et al. [9], by an observation of fluorescence.

These nanoparticles arouse a lot of research interest due to their water solubility, excellent optical properties as photoluminescence, biocompatibility, chemical inertness, low toxicity, easy synthesis, versatile surface functional groups engineering which provides the control of physicochemical properties, chemical and thermal stability and environmental friendliness [10], as schematically reported in figure 1.2 .

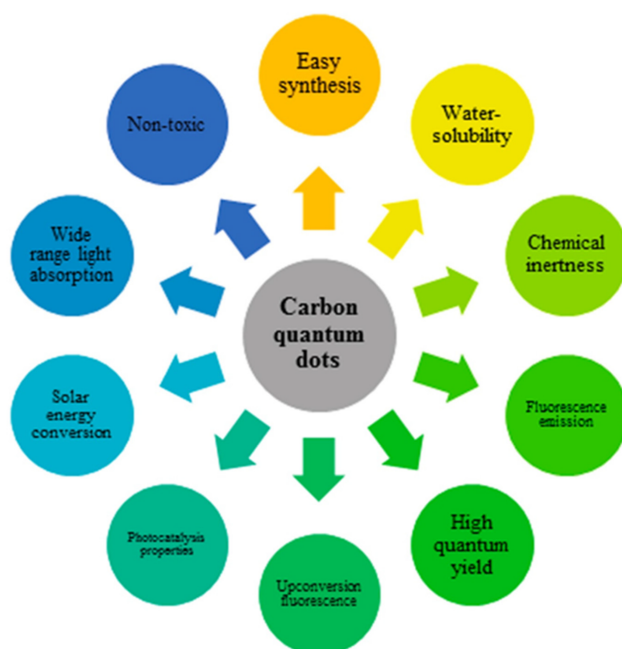


Figure 1.2: Schematic representation of C-Dots advantages that arouse a lot of scientific interest, PL, biocompatibility, solubility, nontoxicity and other.

Despite all these propitious advantages and their potential applications of C-Dots, doubts and controversies arise from the lack of information about the internal structure and difficulty to define electronic properties responsible of their photoluminescent mechanism [11].

These features of C-Dots applications are discussed in detail in the following sections of this chapter.

1.2.1 C-Dots properties and characteristics

C-Dots are discrete zero-dimensional carbon based nanoparticles, since their lateral dimensions are less than 10 nm [12]. From the numerous analyzes arise that they can be amorphous or nanocrystalline and contain sp^2 type carbon clusters with graphitic like core and a functional group shell [13,14]. As many analyzes reveal the possible presence of pure amorphous core with some sp^3 hybridized carbons [12,15,16].

Despite a variety of possible structures, the C-Dots are characterized by a well-ordered almost spherical shape with various oxygen and nitrogen containing species, such as carboxyl (-COOH), carbonyl (C=O), hydroxyl (-OH), amine (-NH₂), and other groups, atoms (N, P and S) and polymeric aggregations on the surface or into their structure, specific of a synthesis method and precursors [17,18]. The surface functionalization provides high biological activity, great water solubility, ability to form conjugates with a variety of organic and inorganic substances and optical properties. C-Dots schematic structure representation is reported below in figure 1.3.

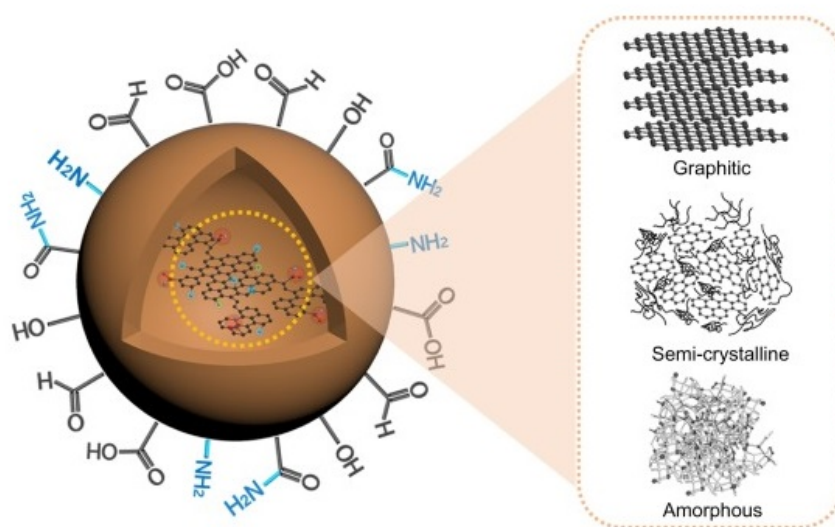


Figure 1.3: Design of C-Dots and their possible classes according to the structural characteristics: graphitic, semi-crystalline and amorphous. [19]

C-Dots can be divided in severe classes according to their hypothesized structural characteristics. One of the possible classifications is [20,21,22]:

- **Graphene quantum dots** possess few layers of graphene with externally connected functional groups. Present an anisotropic structure prepared both with top-down through graphene sheets cutting [23] and bottom-up methods using citric acid and glucose [24,25].

-
- **Carbon nano dots** are mainly spherical and can be formed both by a crystalline graphitic or an amorphous like structures. Some possible subgroups of this class are proposed by Keenan et al. [22]:
 - **Black carbon dots** synthesized through a top-down method by means of acidic oxidation [26]. They were implemented for study of specific drug delivery to bones, delivery across the blood-brain barrier (BBB) and cell penetration [27].
 - **Carbon nitride dots** prepared through a bottom-up microwave assisted method using an acid and an amine. C-Dots so synthesized have showed a great ability to target glioblastoma cells as well as the BBB for drug delivery [28,29].
 - **Yellow carbon dots** are synthesized through bottom-up ultrasonication assisted method using an acid and an amine. using an acid and an amine. They have an excellent penetrating ability, including the central nervous system [30].
 - Other groups which contain **polymer carbon dots** formed by aggregation of polymeric cross linked chains synthesized from m linear polymers or monomers [19,20].

1.3.1.1 Light absorption

As anticipated, optical properties of C-Dots arouse a lot of interest. Despite the fact that C-Dots can be synthesized with different chemical and structural morphologies, most show great absorption properties at ultraviolet radiation wave lengths (UV range) with similar features and a tail that extends to the visible region (VIS range), as could be seen from figure 1.4. The absorbance in a region close to 230 nm approximately is attributed to the $\pi - \pi^*$ transition of the C=C aromatic bond of the C-Dots core characterized with sp^2 hybridized graphitic like structures. While peaks above 300nm are generally refer to $n - \pi^*$ transitions of C=O trapped energy levels in carbon core. $n - \pi^*$ transition occurs at lower discrete energies because it is related to energy levels created inside the HOMO-LUMO gap represented by $\pi - \pi^*$ states. The presence of absorption band above 400nm is attributed to the surface state transition related to C=O and C=N bonds, the red shift is attributed to the aromatic heterostructures containing a N atom. It is due to the fact that nitrogen injects an electron into unoccupied π^* orbital reducing HOMO-LUMO gap and consequentially its transition energy. So, this C-Dots optical property originates from a combination of core and surface transitions, defining high energy absorption [30,31,32]. Surface functional groups has a crucial role in determining the absorption range of C-Dots. Low energy absorption band, above 300nm, may be originated also from interlayer charge transfer phenomena [30]. The absorption properties can be regulated by engineering the surface or by passivation techniques. Besides C-Dots produced from the same precursors but using different synthesis techniques shows different

absorption bands. For example, hydroxyl and carboxyl groups on the C-Dots surface can bring near two energy levels causing red shifted absorption [33]. Since there are still many gaps on the C-Dots structure and origins of the optical properties, the accurate extinction coefficient determination and quantum confinement effect remain a challenge [34].

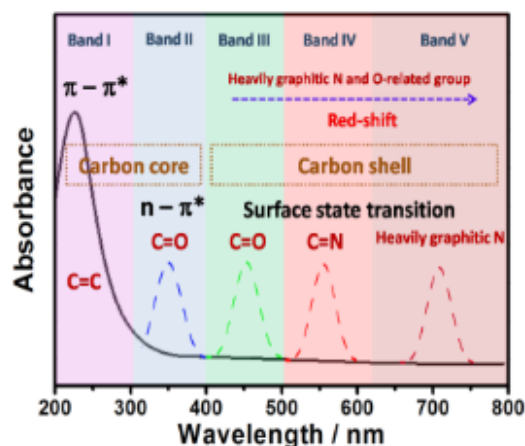


Figure 1.4: Schematic representation of the absorption spectrum and related electron transition of C-Dots [35].

1.3.1.2 Photoluminescence property

Photoluminescence of is one of the most interesting aspects of C-Dots, but it is also a bigger issue on C-Dots properties investigation. The lack of knowledge about C-Dots and their complex structure makes difficult to understand the exact mechanisms behind this phenomenon. Nevertheless, huge number of works were concentrated in order to demonstrate that this phenomenon is excitation dependent and the emission spectrum depends on C-Dots size distribution, surface functional groups and emissive traps [35]. Commonly accepted idea is that the surface is directly responsible for the C-dots PL effect and emissions bands depend on different transitions. The mechanism can be explained by considering that $\pi - \pi^*$ C-dots core energy levels represent HOMO-LUMO gap and trapped energy levels related to defect or functional groups reduce this gap, as in the absorption case. Depending on the specific trapped levels, radiative electron-hole recombination is possible at discrete wave lengths. Oxygen containing surface functionalities (carbonyl, carboxyl and hydroxyl) and nitrogen atoms presented inside the heterocyclic core can tune the emission mechanism through introduction of new (below LUMO and above HOMO) energy trap levels and consequently new electron transitions resulting in red shift [36,37], as schematically represented in figure 1.5. As consequence, PL emission mechanism can be controlled through the surface passivation. Several generated defects (surface oxidation), which reduce HOMO-LUMO gap, trap excitons and are accountable for the red shifted

emission [33].

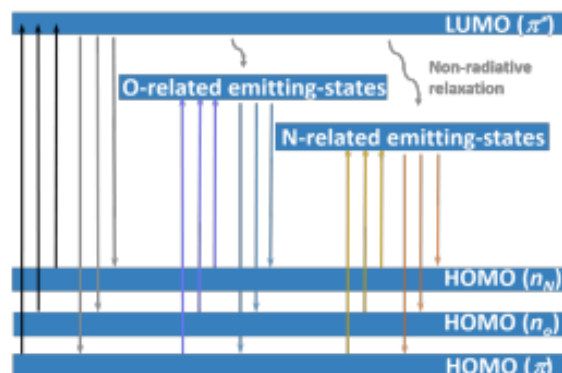


Figure 1.5: Schematic representation of the possible absorption and emission mechanism of C-Dots [35].

Concerning the C-dots dimension, it was observed that C-Dots energy gap decreases as a function of increasing dimensions and anomalous PL behaviour arise from this dependency and corresponding edge state modifications [38,39,40]. So, increasing C-Dots size a red shifted emission can be observed, as shown in figure 1.6. The quantum confinement effect was also analyzed through density function theory calculations (DFT) demonstrating a huge decrease of energy gap with increasing domain size of aromatic benzene rings [41,42,43]. Unfortunately, obtained data have no correspondence with that experimentally obtained, due to other unknown mechanisms implemented in PL phenomenon.

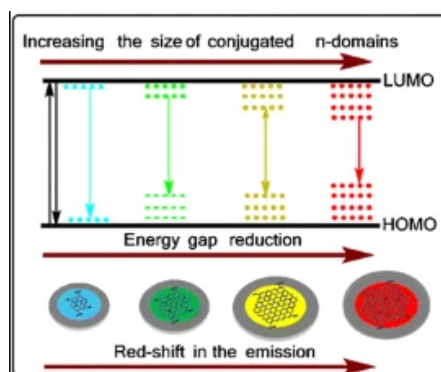


Figure 1.6: Schematic representation of the possible size-dependent PL mechanism of C-Dots [40].

This PL phenomenon is very important in biological real time imaging applications because, differently to the UV radiations, near-infrared waves can easily pass through biological tissues (skin, organs, fluids) providing an excellent imaging implement [44].

1.3.1.3 Non toxicity and Biocompatibility

Biological applications in vivo and in vitro have requirement of biocompatibility and non toxicity of the employed materials. C-Dots, being carbon based nanostructure, are potentially non toxic. This makes them promising materials in bioanalytical purposes replacing some toxic metal based nanoparticles employed in the past [45,46]. C-Dots cytotoxicity was largely in vitro investigated with satisfying results [47]. No inflammation effects were observed in rats liver, kidney or lungs with different dosages of C-Dots over 22 days during the in vivo cytotoxicity studies [48]. A lot of other studies were conducted by the cell viability test in this regard, and demonstrate that C-Dots are characterized by low cytotoxicity and excellent biocompatibility [49]. This makes possible the C-Dots availment in [50,51,52,53,54]. Other studies supported by prothrombin time assays in plasma samples show that C-Dots doesn't promote any blood coagulation [55].

Due to their unique structural characteristics, C-Dots possess other interesting optical properties as up-conversion PL, solid state phosphorescence, aggregation induced phosphorescence and temperature dependent emission [35].

1.3.1.4 Solubility

C-Dots oxygen-containing surface functional groups as carboxyl, hydroxyl and carbonyl favour their solubility in aqueous environment and make possible their application in many biological field [56].

These properties has placed C-Dots as a promising material at center of different fields (figure 1.7) [20] like nanomedicine including cancer photodynamic and radio therapy[57,58], drug delivery [57], chemical sensing of heavy metals [60], biosensing of gene and DNA nucleic acids [53,61], bioimaging of cancer cells and viability as contrast agent [50,51,52,53,54,55,62], protoelectronics [63], photocatalysis [64] and photovoltaics [65].

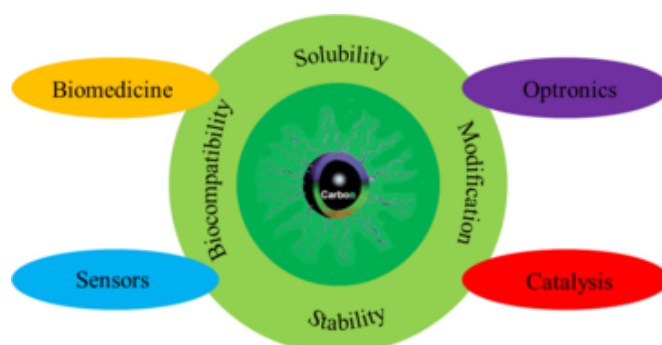


Figure 1.7: C-Dots more promising vanguard applications and vantages: biomedicine, optronics, sensors and catalysis.

1.2.2 C-Dots preparation

The great variety of the proposed synthesis mechanisms for C-Dots can be divided into two main categories: top-down and bottom-up techniques [18,66], schematically represented in figure 1.8.



Figure 1.8: Schematic diagram of the top-down and bottom-up approaches for synthesizing of C-Dots and their precursors [66].

- **Top-down** approaches consist in decomposition of carbon structure which possess a sp^2 carbon structure (graphite, graphene, carbon nanotubes (CNTs) and etc.) into nanoscale particles via harsh chemical, electrochemical and physical methods such as arc discharge, laser ablation, microwave irradiation, electrochemical and chemical oxidation. Reducing size and modulating surface of these sources, their band gap becomes more efficient for PL phenomenon [20].
- **Bottom-up** approaches involve natural fabrication methods based on the synthesis and carbonization from small molecular (amines, organic acids, biomass, carbohydrates etc.) or polymeric precursors under simpler conditions, such as hydrothermal, ultrasonic and microwave assisted reactions, plasma irradiated pyrolysis.

Usually, some post-synthesis optimization procedures, as doping or surface passivation, are implemented in order to preserve, improve or change some of C-Dots properties [26].

An increasing number of researches are concentrated on the sustainability of C-Dots implementing various natural carbon sources in synthesis processes and replacing organic compounds precursors with biomass material [26].

C-Dots synthesized with top-down approaches present high quality and relatively intact structure, while those fabricated by mean of bottom-up approaches are characterized by more amorphous core and great functionalization [20].

Selection of precursors, reaction method and conditions are a critical point in the C-Dots synthesis. These factors strongly affect the size, both the chemical structure and the electrical properties [26]. Lack of complete clarity about C-Dots arouses some issues during the synthesis, as the poor control of the nanoparticles dimension and shapes. Nevertheless, some troubles can be avoid through post process optimization procedures. For example dopping or surface passivation, are implemented in order to preserve or improve some surface properties or to avoid C-Dots aggregation [26,67].

1.2.3 Bismuth Oxide properties and applications

Bismuth (*Bi*) is a 83rd chemical element of periodic table. It is a heavy metal which possess many properties that have led to its use in various scientific and industrial fields. Bismuth is a naturally diamagnetic and one of the less thermal conductive metal [68]. It shows a high electrical resistivity and Hall effect coefficient [69]. However, one of the most interesting property is it unusual for heavy metals low toxicity and high biocompatibility [70,71]. Radiopacity to X-radiation, arising from a high atomic number of Bismuth, is its another crucial feature, indeed Bismuth is used for fabrication of the shields to protecting from X-ray during medical examinations [72].

In the last years, interest of bismuth containing materials was extended to micro and nano scale including many fields, such as medicine, diagnostic, chemistry, optics, electronics and engineering was extended to the micro and nano scale [73,74]. Nanoparticles became promising mainly in medical diagnostics and therapeutics fields [75]. Bismuth and its derivatives were successfully implemented for the fabrication of various micro and nanoparticles with unique characteristics. These particles have a great diversification in terms of chemical composition, structure, morphology, size and shape [76,77]. Bismuth based micro and nanoparticles show good stability, large surface area, predisposition to functionalization [72,78].

The most important and naturally present compound of bismuth is Bismuth Oxide (Bi_2O_3). It is one of the deeply studied bismuth compounds. This semiconductor exhibits excellent electrical and optical properties due to it wide band gap, high dielectric permittivity and refractive index and it is applied in photocatalysis and sensing [79]. Bismuth Oxide nanoparticles posses higher cell penetration capability and less side effects [80]. Great near-infrared absorbance of Bismuth Oxide nanoparticles has great improvements on the radiotherapy and reduces a side effect, instead their radiopacity due to high X-ray attenuation coefficient involve them in radiosensitizing [81].

All these features gave unique performances to the Bismuth based particles and placed they at the center of fields like drug delivery, imaging, biosensing, photothermal and radiation therapy, theranostic and cancer therapy with promising result overcoming some problems related to the other particles [80], schematized in figure 1.9. There are several examples of the Bismuth Oxide nanoparticles biological application, as in vivo X-ray computed tomography [82], imaging and chemo-photothermal combining therapy [83], regenerative medicine as bone engineering and the fabrication of biosensors [78] and many others real examples. Great antibacterial effects were observed also for low concentrations of nanoparticles, as in vitro treatment of chronic osteomyelitis, a bone infection caused by bacteria [84]. Also a fungicidal and antiviral activity was detected [81].

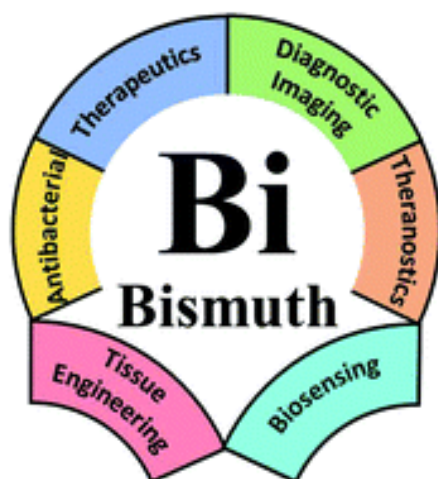


Figure 1.9: Overview of the biomedical applications of Bi nanoparticles: drug delivery, cancer therapy, bioimaging, theranostic, antibacterial uses and bone engineerin. [78]

Even if Bismuth is intrinsically nontoxic material, it is commonly known that nanoparticles can penetrate through biologic barriers and cells membrane, deposit into different organs and cells causing toxic effects including DNA damage, morphological changes, oxidative stress and even cell death [75]. This phenomena are mainly due to the high biological activity of the nanoparticles arising from their reduced size and high surface/volume ratio. So, the crucial point is to design non toxic nanoparticles in order to explore their contribution to biomedicine, drug delivery and diagnostics.

Unfortunately, there is a huge number of uncertainties regarding toxic effects of bismuth based nanoparticles on the human health. As F.Thomason et al. [85] reported in their work, some of the observed toxic effects are attributed to Bi-based nanoparticles, such as encephalopathy, nephropathy, osteoarthropathy, gingivites, stomatitis, colitis and hepatitis, each of which is related to a specific bismuth compounds.

Concerning Bismuth Oxide nanoparticles, several in vitro studies have been done on cytotoxicity, genotoxicity, oxidative stress, apoptosis, hepatocarcinoma, epithelial, adenocarcinoma, carcinoma and toxic effects they cause in liver, kidney, intestine, lung and mammalian cells, and deriving from the exposure to Bi_2O_3 nanoparticles. Cytotoxyc and genotoxic effects were easily demonstated for these samples [85]. However, there are no in vivo evidences of these effects, more studies are needed in order to completely understand Bismuth based nanoparticles. These issues are related in part to the non degradable nature of Bismuth Oxide nanoparticle [86]. A smart solution to improve the Bi_2O_3 biomedical performances consist in covering the surface of these nanoparticles with biocompatible polymers (PEG, PVP) or other particles as carbon based structures. This will improve the colloidal stability in aqueous solutions favouring blood circulation time essential for pharmacokinetic and reduce in vivo toxic effects during drug delivery. Long blood circulation will improve cancer therapy and imaging due

to promoting tumor accumulation. Furthermore, the surface functionalization promotes also a drug delivery system [87].

Although side effects, Bismuth Oxide nanoparticles remains the most promising tool for the theragnostic applications, since they combine radiopacity and cytotoxicity and drug delivery system.

1.2.4 Bismuth Oxide micro and nano particles preparation

Concerning the Bismuth Oxide, in the past years sever methods were implemented for micro and nanoparticles synthesis. The most common fabrication methodologies are hydrothermal, solvothermal, ionothermal, sol-gel, solid state, microemulsion, microwave irradiation and laser used synthesis [78].

Solvothermal synthesis uses an organic solvent instead of aqueous solution like in a the previous one.

Ionothermal synthesis implies the ionic liquids as a solvent media during the micro and nanoparticles fabrication reactions.

Solid state method is a simple solvent free technique that controls the synthesis process through thermal decomposition using different calcination temperature.

Sol-gel method is widely used for synthesis of the sub-micron metal oxide particles with good homogeneity. It consist in two phases, the colloidal suspension of particles and gelation through interconnected network of particles. Subsequently, a sol-gel precursor can be treated thermally, through spinning or electrospinning.

Microemulsion technique consists in an organic phase that contains nanodroplets of water embedded by an active surfactant. These microemulsions contain metal salts and favour the synthesis of the micro and nanoparticles. This is a good method for simultaneous growth and stabilization of particles limiting their size.

Microwave irradiation synthesis is very simple, but efficient method to fabricate micro and nanoparticle with high purity and narrow size distribution. This method can be combined to the hydrothermal one in order to decrease the synthesis temperature.

Sonochemical synthesis implies high-intensity ultrasounds that induce the hot spots with high temperature and pressure. This method takes advantages from phenomena of acoustic cavitation and nebulization.

Laser assisted technique exploits the lase beam to vaporize or ablate the Bismuth in aqueous solutions.

Not only the synthesis method, but also the presence of different surfactants, as PEG and PVP, can affect the shape and size of Bismuth Oxide micro and nanoparticles [83].

CHAPTER 2

Materials and Methods

2.1 Materials

Citric acid was bought from Nortem Biotechnology, p-Phenylenediamine was bought from Fluka, Polyethylene glycol 4000 was bought from PHU Alpaca, sodium lauryl sulfate was bought from Carlo Erba Reagents, lauric acid was bought from Sigma-Aldrich, polyvinylpyrrolidone was bought from Alfa Aesar, Bismuth Nitrate pentahydrate was bought from Fluka, Bismuth Oxide was bought from Fluka, Nitric Acid was bought from Sigma-Aldrich, Sodium hydroxide was bought from Fluka.

All chemicals were used without any purification.

The used instruments for the synthesis and conjugations were: a Vibra Cell sonicator, a hot plate with magnetic stirring, a microcentrifuge MPW-55, a muffle furnace, a tubular Pyrex reactor, ultrasonic bath Elma Elmasonic S15H, electronic balance and a pump.

The C-Dot samples were analyzed through Fourier-transform infrared spectroscopy (FT-IR), Raman spectroscopy, photoluminescence spectroscopy and absorption spectroscopy. The Bismuth Oxide based nanoparticles were analyzed through Field emission scanning electron microscopy (FESEM) and Raman spectroscopy. Finally, the conjugations were examined through Field emission scanning electron microscopy (FESEM), Fourier-transform infrared spectroscopy (FT-IR), Raman spectroscopy, photoluminescence spectroscopy and absorption spectroscopy.

Raman analyses were performed by the Renishaw inVia InSpec confocal microscope using the green wavelength (514nm) of the laser. FT-IR analyses were performed by the Nicolet 5700 FT-IR Spectrometer from Thermo Fisher Scientific. Photoluminescence spectra were created by the PerkinElmer LS-55 fluorescence spectrometer. And finally, UV/VIS absorbance spectra were made by the PerkinElmer UV/VIS spectrometer. And finally, FESEM analysis were performed by ZEISS Supra 40 Field Emission Scanning Electron Microscopy. Schematic representations of the reactions were realized using ChemDraw software.

2.2 Synthesis of C-Dots

In order to prepare C-Dots, 0.56 of p-Phenyldiamine (DPA) was mixed with 0.04g of Citric Acid (CA) in 10ml of DI water and then sonicated for 1 h at 42 kHz (subsequence of 10s and 5s of on and off) promoting in this way the aromatic heterocyclization (figure 2.1). After the reaction, the solution color was purple and the mixture was dried in the furnace at 80°C until the water has completely evaporated. Another set of C-Dots synthesis was repeated including PEG as a reagent and adding it in 1:1, 0.5:1 and 0.1:1 proportions with respect to Citric Acid. At this point, two different methods were used for the C-Dots purification.



Figure 2.1: C-Dots formation mechanism through sonication steps using CA and DPA.

2.2.1 Thermal treatment and purification by centrifugation

Before the thermal treatment, the precipitate was pestled in a mortar to avoid the aggregations facilitate the carbonization process. The previously obtained samples of not purified C-Dots were heated to 250°C, 350°C and 450°C by means of a muffle furnace inside a tubular reactor under argon gas. In this way the C-dots condense and nucleization takes place due to the reorganization of the structure. After 10 minutes, the C-Dots were extracted and cooled to room temperature. Subsequently they were dissolved in deionized (DI) water for 15 min in an ultrasonic bath in order to promote their dissolution and break any aggregations. In order to purify C-Dots, the solution thus obtained was centrifuged at 10000 rpm for 15 min. The main steps of this procedure are reported in figure 2.2. Only the solubilized part was taken and oven dried, instead the residue was removed away. In this way, only the soluble C-Dots were preserved, since they only are

useful in this work. The heat treatment for C-Dots which includes PEG reagent was done only for 250°, instead all the other steps were unchanged. All thermally treated and centrifugated C-Dots are reported in table 2.1.

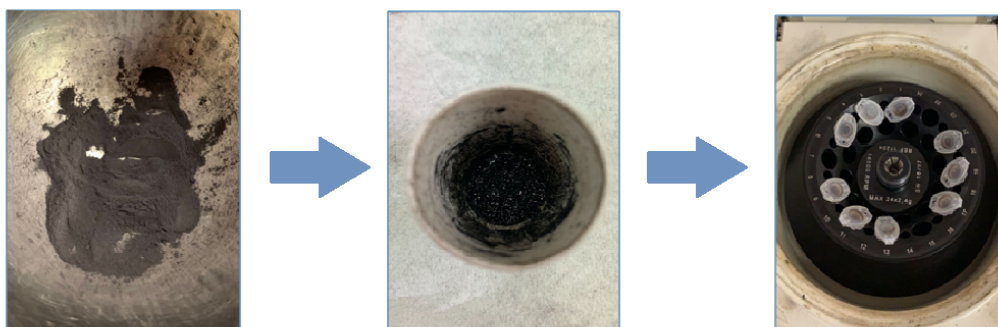


Figure 2.2: C-Dots thermal treatment and purification by centrifugation steps.

C-Dots Thermal treatment and Centrifugation			
Name	Precursors	Surfactant	Annealing T (C)
SP1	DPD, AC	-	-
SP2	DPD, AC	-	250°
SP3	DPD, AC	-	350°
SP4	DPD, AC	-	450°
SP5	DPD, AC	PEG-4000 (1:1 to CA)	-
SP6	DPD, AC	PEG-4000 (1:1 to CA)	250°
SP7	DPD, AC	PEG-4000 (0.1:1 to CA)	250°
SP8	DPD, AC	PEG-4000 (0.5:1 to CA)	250°

Table 2.1: Set of prepared C-Dots thermally treated at different annealing temperatures and containing PEG

2.2.2 Purification by dialysis

The dehydrated precipitate of C-Dots was pestled in a mortar and subsequently 800mg of the C-Dots powder and 6mL of DI water were dissolved and treated in a ultrasonic bath for 15 min. For this type of purification C-Dots prepared with and without surfactant (PEG-4000 1:1 to CA) were used. Then, the purification

was performed by putting the previously obtained solution inside the dialysis membrane (4000 molecular weight cutoff was used) and agitated for 48 h in the water that was changed after 24 h. Dialysis steps are reported in following figure 2.3. The same procedure was done for the not dehydrated C-Dots precursor with and without PEG-4000 (0.5:1 to CA). For the complete characterization and comparison of differently synthesized C-Dots, the dialysis was performed also for C-Dots thermally treated at 250°, with PEG-4000 (0.5:1 to CA) and without it. Finally, the content of the membrane was recovered and oven dried until the water has completely evaporated. All dialyzed C-Dots are reported in table 2.2.

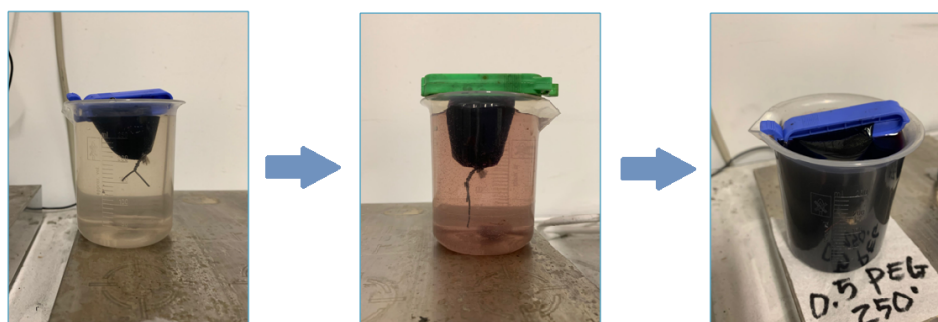


Figure 2.3: C-Dots purification by dialysis steps: (a) at the beginning, (b) after 30min, (c) after 24h.

C-Dots Purification by Dialysis			
Name	Precursors	Surfactant	Annealing T (C)
SP9	DPD, AC	-	-
SP10	DPD, AC	-	250°
SP11	DPD, AC	PEG-4000 (0.5:1 with CA)	-
SP12	DPD, AC	PEG-4000 (0.5:1 with CA)	250°
SP13	DPD, AC	-	dehydrated at 80°
SP14	DPD, AC	PEG-4000 (1:1 with CA)	dehydrated at 80°

Table 2.2: Set of prepared C-Dots dialyzed thermally treated or not and containing PEG.

2.3 Synthesis of Bismuth Oxide base microparticles

In order to have more possibilities in choosing a molecule that best suit several requirements, Bismuth Oxide based microparticles (Bi_2O_3) were prepared using different reagent and methods. They are treated more in detail in the following subsections.

2.3.1 Hydrothermal synthesis

One of the applied approaches for synthesis of the Bismuth Oxide microparticles was a hydrothermal reaction using Bismuth Nitrate and Nitric Acid as precursors. 4g of Bismuth Nitrate pentahydrate ($Bi(NO_3)_3 \times 5H_2O$), 30mL of DI water and approximately 2mL of Nitric Acid (HNO_3), which promotes Bismuth Nitrate solubility, were stirred at $80^\circ C$ until the Bismuth Oxide was totally dissolved. Then Sodium Hydroxide ($NaOH$) was added at room temperature, to avoid exothermic behaviour, until the solution reached approximately 10pH and an white precipitate of the Bismuth Hydroxide ($Bi(OH)_3$) was formed. Finally the solution was stirred at $80^\circ C$ for 3h and the Bismuth Hydroxide was decomposed in Bismuth Oxide yellow precipitate, which was filtered and oven dried at the end of the synthesis (figure 2.4). All the steps were repeated including into the preparation also four different active surfactants (sodium lauryl sulphate (SLS), lauric acid (LA), polyethylene glycol (PEG-4000) and polyvinylpyrrolidone (PVP)) in 5% by weight of bismuth present in $Bi(NO_3)_3 \times 5H_2O$. In order to study the effect of an active surfactant on the morphology and size of the Bi_2O_3 particles, the synthesis was also implemented using 10% by weight of bismuth of PEG-4000. Set of hydrothermally synthesized Bismuth Oxide microparticles is reported in table 2.3

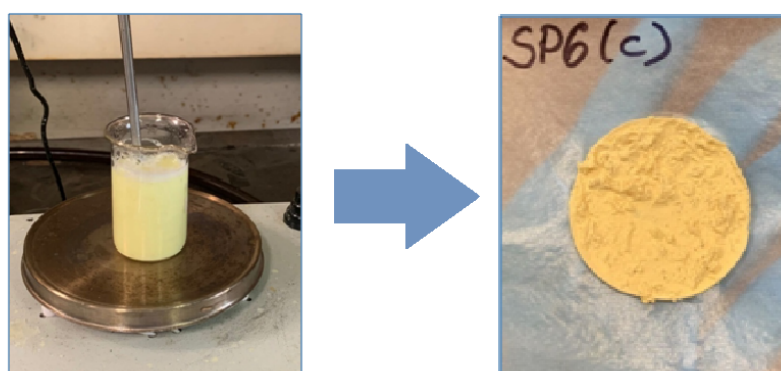


Figure 2.4: Hydrothermal Bismuth Oxide synthesis from Bismuth Nitrate: (a) during reaction, (b) after filtering the product.

Hydrothermal Synthesis			
Name	Precursors	Active Surfactant (AS)	
		Type	wt %
SP16	$Bi(NO_3)_3 \times 5H_2O, HNO_3, NaOH$	-	-
SP17	$Bi(NO_3)_3 \times 5H_2O, HNO_3, NaOH$	SLS	5%
SP18	$Bi(NO_3)_3 \times 5H_2O, HNO_3, NaOH$	PEG-4000	5%
SP19	$Bi(NO_3)_3 \times 5H_2O, HNO_3, NaOH$	PVP	5%
SP20	$Bi(NO_3)_3 \times 5H_2O, HNO_3, NaOH$	LA	5%
SP22	$Bi(NO_3)_3 \times 5H_2O, HNO_3, NaOH$	PEG-4000	10%

Table 2.3: Set of hydrothermally synthesized Bismuth Oxide microparticles with active surfactant:SLS, PEG-4000, PVP, LA.

2.3.2 Solid state synthesis

The solid state syntheses were performed starting from Bismuth Nitrate pentahydrate ($Bi(NO_3)_3 \times 5H_2O$) without solvent. Thermal decomposition of this salt is carried out using different calcination temperatures in a gradual way inside a tubular reactor in inert ambient (figure 2.5). Two samples were obtained with this approach using 30g and 15g of Bismuth Nitrate, one following steps of 200°C for 1h, 300°C for 2h, 425°C for 2h. Table 2.4 reports Bismuth Oxide based microparticles through solid state synthesis.

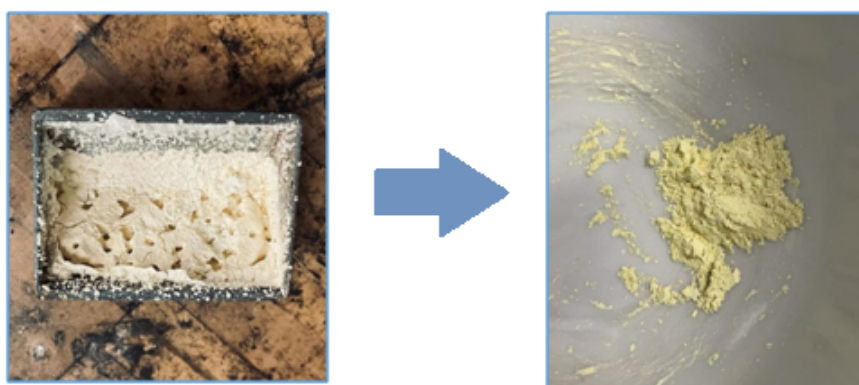


Figure 2.5: Solid State Bismuth Oxide synthesis: (a) at the end of synthesis, (b) after cooling.

Solid State Synthesis				
Name	Material	Step 1	Step 2	Step 3
SP23	$Bi(NO_3)_3 \times 5H_2O$	1h at 200°C	2h at 300°C	2h at 450°C

Table 2.4: Set of hydrothermally synthesized Bismuth Oxide microparticles with active surfactant:SLS, PEG-4000, PVP, LA.

2.4 Synthesis of Bismuth Oxide and C-Dots conjugations

Several conjugation attempts were performed between C-Dots and Bismuth Oxide based microparticles in order to test different interactions, characteristics and performances. As conjugation technique the dispersion of microparticles in aqueous solution of C-Dots was used.

2.4.1 Solid state Bismuth Oxide based particles with different types of C-Dots

The conjugations of two finished reagents, Bismuth Oxide based microparticles prepared by solid state technique, and a set of different samples of purified C-Dots were done. C-Dots included those thermally treated at 250°C and 450°C, containing PEG-4000 (0.1:1 and 0.5:1 to CA) and dialyzed with PEG-4000 (0.5:1 to CA) treated at 250°. 50mg of the Solid State prepared Bismuth Oxide particles were mixed with 50mg of each sample of a purified C-Dots considered set and 50mL of DI water. These samples were agitated by means of a plate with magnetic stirring for 48h and subsequently centrifuged for 15 min. Finally the precipitate was separated from the solution and both were oven dried. Schematic representation of the conjugation is reported in figure 2.6.

2.4.2 Hydrothermally prepared Bismuth Oxide microparticles with different types of C-Dots

The previous conjugation method was repeated also for hydrothermally prepared Bismuth Oxide microparticles with PEG-4000 as active surfactant at 5% wt. and a set of C-Dots. More precisely dialyzed C-Dots (with and without PEG-4000 0.5:1 to CA and previously thermally treated), thermally treated at 250°C only with and without PEG-4000 (0.5:1 to CA). Also hydrothermal Bismuth Oxide microparticles synthesized with 10% wt. were conjugated with thermally treated containing PEG-400 (0.5:1 to CA) dialyzed and not C-Dots.

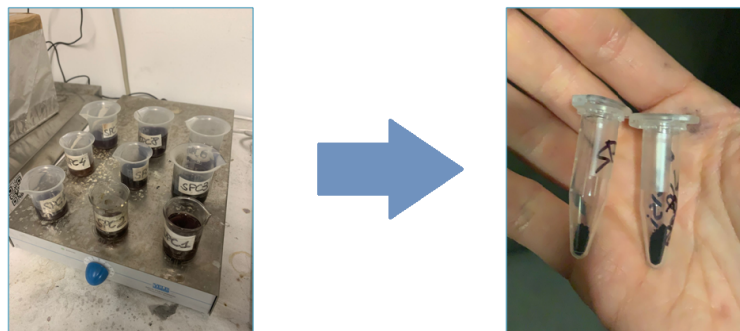


Figure 2.6: Conjugation between C-dots and Bismuth Oxide microparticles through stirring: (a) during the conjugation, (b) after centrifugation and dehydration of residue and soluble part.

2.4.3 Direct synthesis of Bismuth Oxide microparticles and conjugation with C-Dots

The simultaneous preparation of particles and their direct conjugation with C-Dots was implemented. 2g of not purified C-Dots without PEG-4000 were mixed with 200mg of Lauric Acid, in order to favour the following conjugation, and 15ml of DI water and then sonicated for 15 min. After this, the hydrothermal synthesis approach was repeated adding the previously treated C-Dots after the Bismuth Hydroxide precipitation and carrying on the reaction for 3h at 80°C with the final creation of a green precipitate, as shown in figure 2.7. The obtained product was filtered and subsequently oven dried.

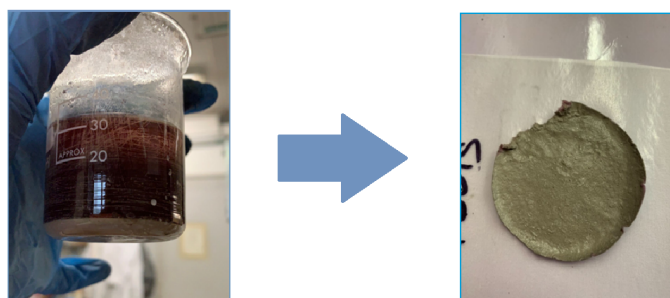


Figure 2.7: Hydrothermal synthesis and direct conjugation of Bismuth Oxide microparticles with C-Dots starting from Bismuth Nitrate: (a) during conjugation (b) after filtering.

All obtained conjugation are reported in table 2.5.

Conjugations C-Dots and Bismuth Oxide based Microparticles		
Name	C-Dots	Bismuth Oxide Microparticles
SP25	SP2	SP23
SP26	SP4	SP23
SP27	SP8	SP23
SP28	SP7	SP23
SP29	SP12	SP23
SP30	SP10	SP18
SP31	SP11	SP18
SP32	SP12	SP18
SP33	SP9	SP18
SP34	SP2	SP18
SP35	SP8	SP18
SP36	SP13	SP22
SP37	SP8	SP22
SP38	C-Dots precursor, 10% of LA	$Bi(NO_3)_3 \times 5H_2O$, NHO_3 , $NaOH$

Table 2.5: Set of conjugation obtained by combining more promising C-Dots and Bismuth Oxide microparticles.

CHAPTER 3

Results and Discussions

3.1 C-Dots

The whole set of fabricated C-Dots was prepared through a bottom-up method using precursors CA, p-DPA, and in some cases surfactant PEG-4000. Their chemical structures are reported in the following figure 3.1

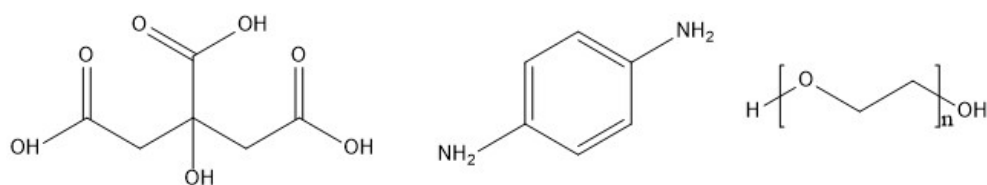


Figure 3.1: Precursors used for C-Dots synthesis. From left to right: CA, DPA and PEG-4000.

C-Dots were synthesized following the procedure described in the work of Mintz et. al [22] for Y-CDs, with the difference of using p-Phenylenediamine instead of o-Phenylenediamine. The supposed growth mechanism is described in the following schematic representation in figure 3.2:

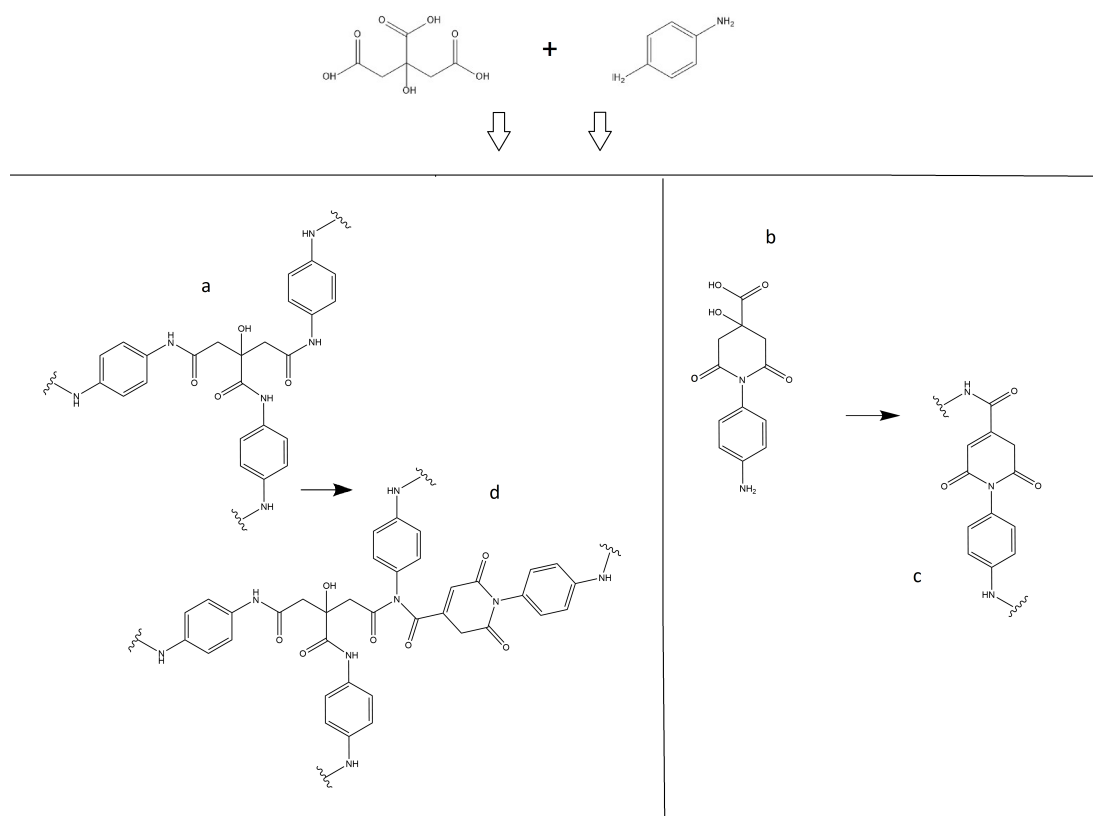


Figure 3.2: Possible growth mechanisms of the synthesized C-Dots

The choice of an aromatic amine as a precursor is crucial. Sonication of these precursors promotes the aromatic heterocyclization through high-intensity ultrasonounds that induce the hot spots with high temperature and pressure. One of the possible reactions is obtained by the initial formation of the derivatives of amide from AC and PDA reaction. This occurs through the amidation of the AC carboxylic groups, which will not be free anymore, with the PDA amino groups and its subsequent transformation in the random cross-linked polymer structure figure 3.2(a). The main contribution of the carbonyl groups of CA is to provide a great number of unsaturated carbons, which favour the conjugations with other particles due to their π bonds. The reaction of PDA amine groups (each of these have two growth points) awards more ordered and condensed structure. It is possible that the PDA amino groups react with an amino group of another PDA molecule or with two carboxyl groups of CA molecule forming a cyclic unsaturated amine, figure 3.2 (b, c), with functionalities as carboxil groups and PDA residue. The CA hydroxyl groups favour a heterocyclic structure containing N atom due to their elimination reaction. This can react with carboxyl group of CA forming more complex structure and so on (d). So, C-Dots of this synthesis are randomly cross-linked heterocyclic structures containing N atoms (which amount is a function of preparation setup) which are organized in parallel planes with external functional groups. Increasing the reaction temperature these

decarboxylation and dehydration processes are further favored and the structure aromatization is promoted.

3.1.1 FT-IR spectroscopy

Through FT-IR spectroscopy of C-Dots it is possible to identify several characteristic absorption bands related to the bonds stretching and bending. C-Dots IR spectrum is good tool to investigate and compare different structural and chemical composition of C-Dots prepared with different synthesis methods and/or reagent. Firstly, it is possible to understand the C-Dots growth mechanism and extract some information about the final structure by comparing precursors spectra. The following figure 3.3 reports IR spectra of CA, DPA and C-Dots as a result of their sonication.

Starting from the lower energies, CA presents a peak at 3500cm^{-1} and a band approximately between 3000 and 3500cm^{-1} , former related to the hydroxyl ν_{OH} and later to the carboxylic band one. Carboxyl ν_{OH} has lower reduced mass, so it is collocated at higher energies (lower wavenumbers). The hydroxyl ν_{OH} has a shoulder indicating the fact that two interactions are possible, hydroxyl OH with carboxyl OH or with another hydroxyl OH. Different intensities of these two peaks indicate that the first one is more probable (3:1 proportionality). On the other hand, the carboxyl OH band is a result of the presence of three distinguished peaks since CA molecule contains three carboxylic groups, one at the center and two on the sides. These can interact one with each other combining in three different ways: side-side, side-center and center-center. Also in this case the relative intensities of three peaks represent probabilities of these reactions. The peak related to the saturated ν_{C-H} is present between 2750 and 2950cm^{-1} , but its intensity is very low since this type of bond has low dipole momentum. $\nu_{C=O}$ is reported approximately in region of $1680 - 1800\text{cm}^{-1}$ by two intense peaks, indicating the high polarity of momentum of these bonds. Two peaks are related to two possible types of interaction: carboxyls with others carboxyls or hydroxyl OH.

Now, analyzing p-DPA IR spectrum, the peaks related to the ν_{N-H} can be observed between $3200 - 3400\text{cm}^{-1}$. The highest one on the right corresponds to the primary amine and the others to secondary and tertiary respectively. Approximately at 2950cm^{-1} it is possible to observe the unsaturated ν_{C-H} characteristic of the aromatic compounds. Its intensity is higher with respect to saturated one due to the higher polarity of this bond. Between $1600 - 1700\text{cm}^{-1}$ there are two peaks representing the δ_{C-N} relative to two resonance structure configurations. The most intense peak at 1500cm^{-1} is the so called ring breathing, it indicates the the $\nu_{C=C}$, typical footprint of aromatic structures. The last analyzed peak is that at 1250cm^{-1} representing ν_{C-N} .

Comparing C-Dots with the spectrum of AC, it can be notice that the sign related to the hydroxyde OH groups at 3500 cm^{-1} disappears, so the AC has react. Also the peak related to the saturated ν_{C-H} decreases in intensity, indicating the formation of aromatic structures. The peaks representing the $\nu_{C=O}$ of the carboxyl group disappears because reacting with amino groups of DPA, the free carboxyl group concentration decreases.

Instead comparing the obtained C-Dots with DPA spectrum it can be noticed the peak indicating $\nu_{C=C}$ remains. Moreover, its splitting in at least two component suggests the heterocyclicity of precursor (the left one indicates the presence of one atom of N inside the ring). Also the peaks characteristic of ν_{N-H} change their proportions and intensity, due to the reaction between amino groups of DPA and carboxyl groups of AC, transforming them into amides.

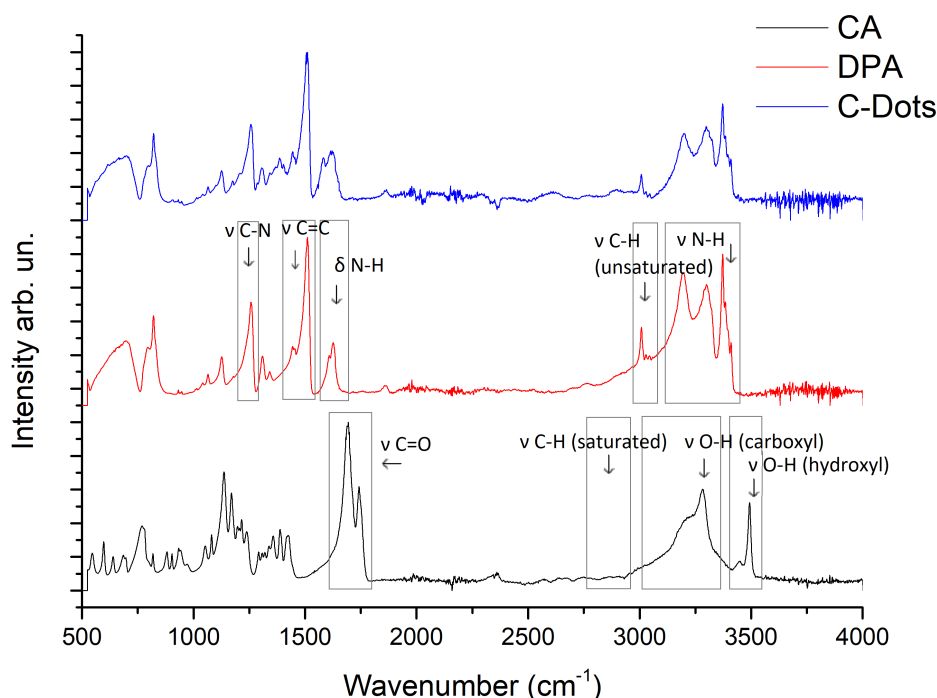


Figure 3.3: Comparison of IR spectra of CA, DPA and not purified C-Dots.

Subsequently, FT-IR spectroscopy was implemented to investigate the structure evolution of C-Dots thermally treated at different temperature. From the comparison of spectra obtained for different samples in figure 3.4 it can be deduced that, by increasing the annealing temperature, peaks of the ν_{N-H} change further their relative intensities. The primary amine peak decreases in favor of the secondary and ternary amine, confirming that thermal treatment promotes the amidation and creates more ordered and condensed configurations through the nucleation. The structure redistribution is deduced also from the increasing

intensity of the $\nu_{C=C}$ and that of unsaturated ν_{C-H} , both characteristic of the aromatic ring structures, which demonstrate that the C-Dots structure becomes more and more aromatic by increasing annealing temperature.

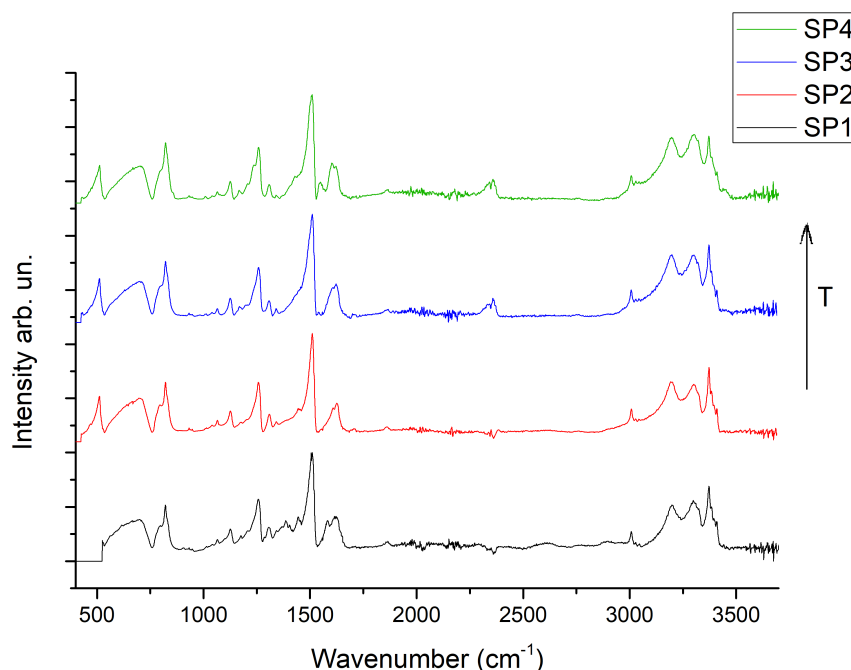


Figure 3.4: IR spectra of thermally treated C-Dots: SP1 not thermally treated, SP2 at 250°C, SP3 at 350°C and SP4 at 450°C.

Now, the benefits of dialysis purification on the C-Dots are analyzed through a set of FT-IR spectra reported in figure 3.5. The same, but more evident, structure redistribution can be observed also for C-Dots purified by dialysis. From the comparison of two purification methods in figure 3.6 it arises that the heat treatment results in a more heterogeneous and disordered structure with many external functional groups, instead the dialyzed one has more compact structure, less flexible with an intense signal of $\nu_{C=C}$ and unsaturated ν_{C-H} , typical of the aromatic rings. Thanks to dialysis also the expulsion of free amines occurs, as can be seen from the disappearance of primary amine stretching peak. An important aspect arises from the fact that the skeletal vibrational modes, below 1000cm^{-1} , are drastically inhibited, differently to the thermally treated C-Dots. This indicates that the structure is very rigid, like a graphitic one, and its functionalizations are lost. The purification by dialysis can be explained through the concept of osmosis. Due to the pressure gradient established between inside and outside of the membrane the precursor is purified, proportionally to the membrane cutoff, from the too small organic molecules and oligomers which did not polymerize in the previous steps [88]. So, the dialysis purification is more effective with respect to the thermal treatment and centrifugation. It is possible to choose the method to use basing on the properties one wants to get.

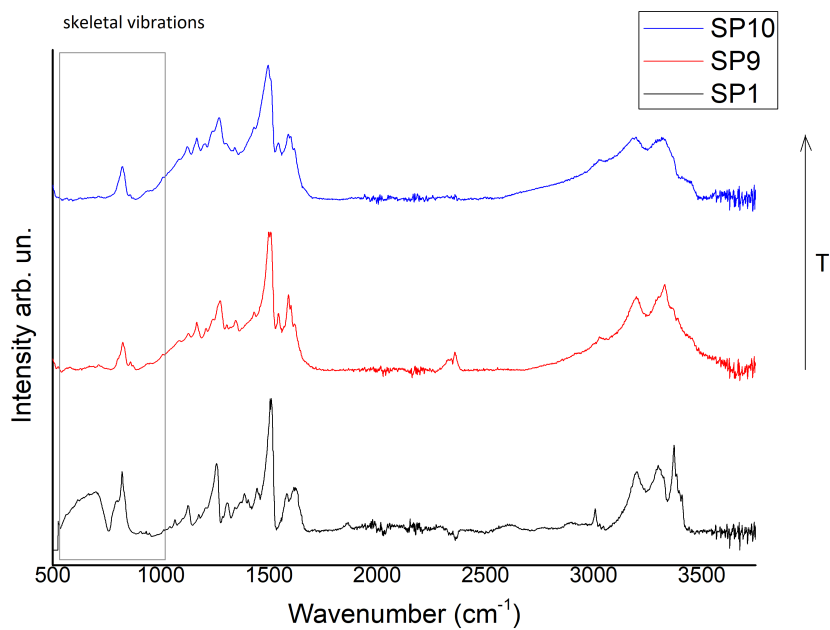


Figure 3.5: IR spectra of dialysed C-Dots: SP1 not purified, SP9 dialyzed and SP10 thermally treated at 250°C and dialyzed.

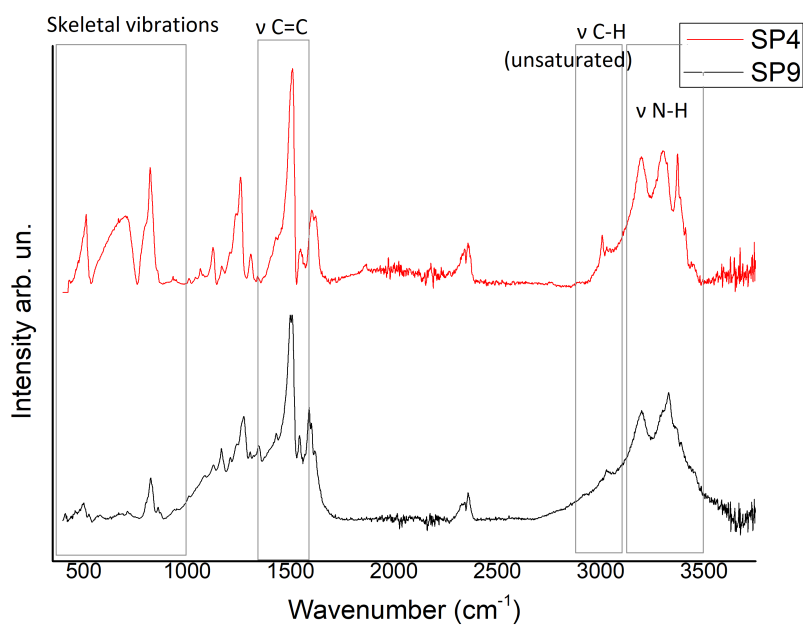


Figure 3.6: IR spectra comparison between dialysed C-Dots (SP9) and thermally treated at 450°C (SP4).

If combined, the two nucleation techniques can provide their respective benefits to C-Dots. From figure 3.6 representing SP9 and SP10 can be seen that, in addition to dialysis effects, the thermal treatment at 250°C changes the proportionalities of the peaks relative to the ν_{N-H} promoting the amidation and aromatization.

Observing the spectrum of C-Dots containing PEG-4000 in figure 3.7, it can be noticed that increasing PEG-4000 concentration enhances the $\nu_{C=C}$ of the aromatic ring. Also the peak of the saturated ν_{C-H} is increased due to its presence in PEG-4000, but it decreases its intensity after a thermal treatment due to the reasons discussed before. This result can be explained by the fact that PEG-4000 creates micella in aqueous phase, acting as a separator which avoids the C-Dots aggregation, favors the aromatic compounds condensation and reacting with its functional groups will maximizes the subsequent conjugation. Samples containing PEG-4000 were treated only at 250°C in order to stay below its degradation temperature, which depends on an average molecular weight of polymers [89].

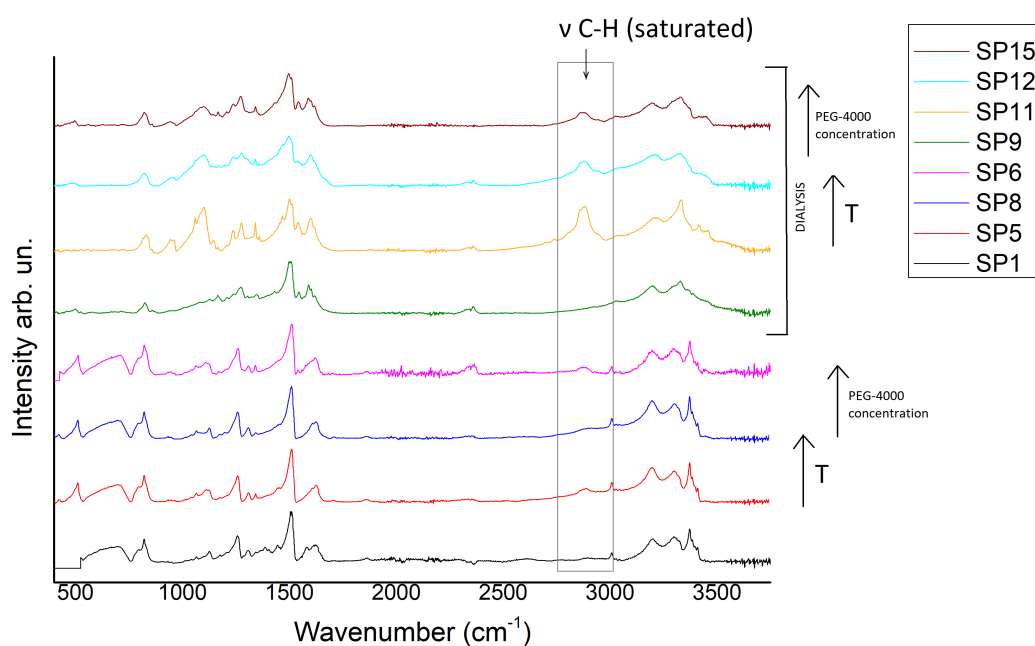


Figure 3.7: IR spectra comparison of C-Dots containing PEG, thermally treated or dialyzed: SP1 not treated without PEG, SP5 not treated with PEG (1:1 to CA), SP8 thermally treated with PEG (0.5:1 to CA), thermally treated with high PEG concentration (1:1 to CA).

3.1.2 Raman spectroscopy

Each of the synthesized C-Dots samples were analyzed through Raman spectroscopy in several points showing a good uniformity since the obtaining spectra are quite similar. Analyzing the obtained Raman spectrum for different samples of thermally treated C-Dots it can be observed that the C-Dots synthesized in this way present a number of well defined peaks, but their interpretation is very challenging due to their high fluorescence. Photoluminescence is shown in figure 3.8 as a rising slope of the Raman signal, deriving from the presence of several functional groups on the C-Dots surface. So, even if the low intensity laser is used, the ration signal/noise remains low covering a part of the bands.

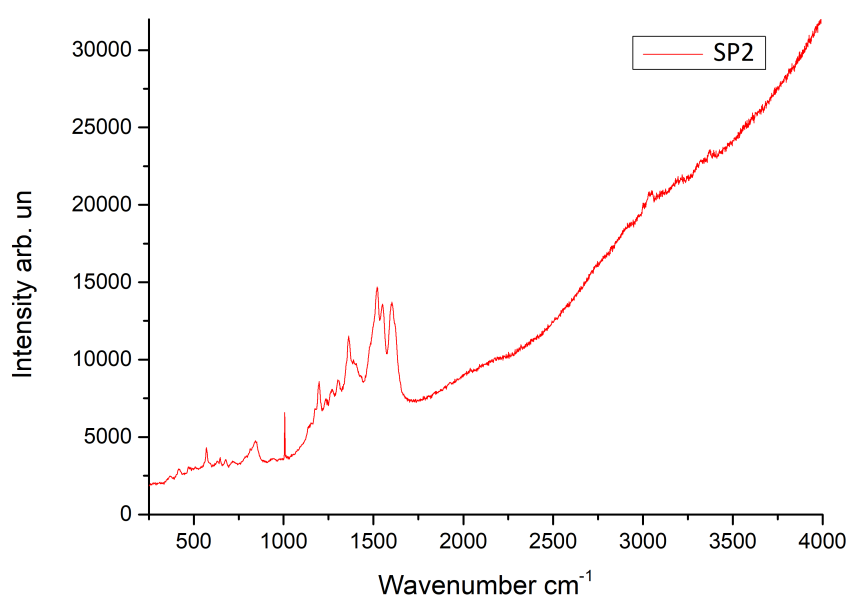


Figure 3.8: Proof of C-Dots photoluminescence from Raman spectrum of thermally treated (250°C) C-Dots.

All poly-aromatic species contain D and G bands in their Raman spectra. D-band intensity is related to the size of graphitic sp^2 hybridized regions being attributed to the breathing modes of sp^2 atoms in rings. While G band is attributed to the bond stretching of all pairs of sp^2 atoms in both rings and chains. Therefore, in regions around 1360cm^{-1} and 1560cm^{-1} , commonly attributed to the D and G [90,91], there are a great number of peaks as can be seen in figure 3.9. So, the identification of these bands in synthesized C-Dots can be only supposed without any certainty on their effective position due to low intensity. These bands indicate that the localized graphitic like nanostructures are formed in C-Dots core, but at the same time they are disordered and heterogeneous. Large band present between 2500 and 3500 cm^{-1} is related to the hydroxyl group

and indicates that others oxyhydrogenated carbon compounds are also present.

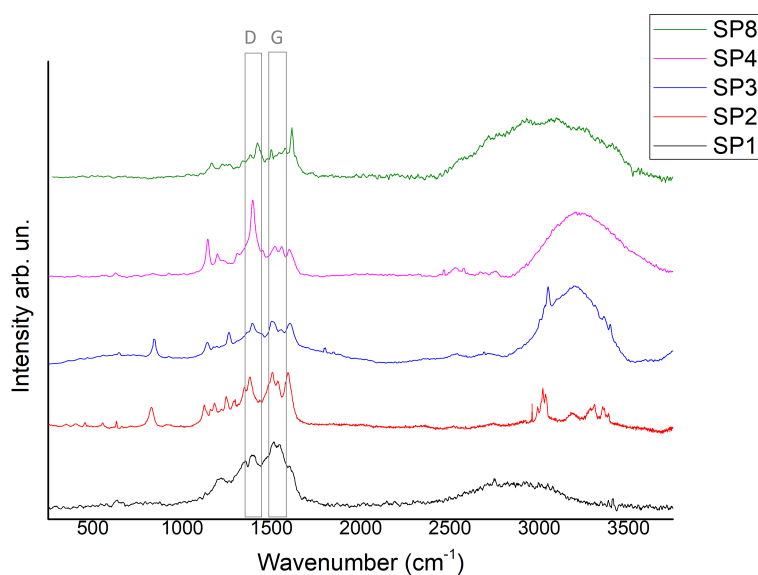


Figure 3.9: Raman spectra of thermally treated C-Dots: SP1 not treated C-Dots, SP2 thermally treated at 250°C , SP3 thermally treated at 350°C , SP4 thermally treated at 450°C , SP8 thermally treated at 250°C containing PEG (0.5:1 to CA).

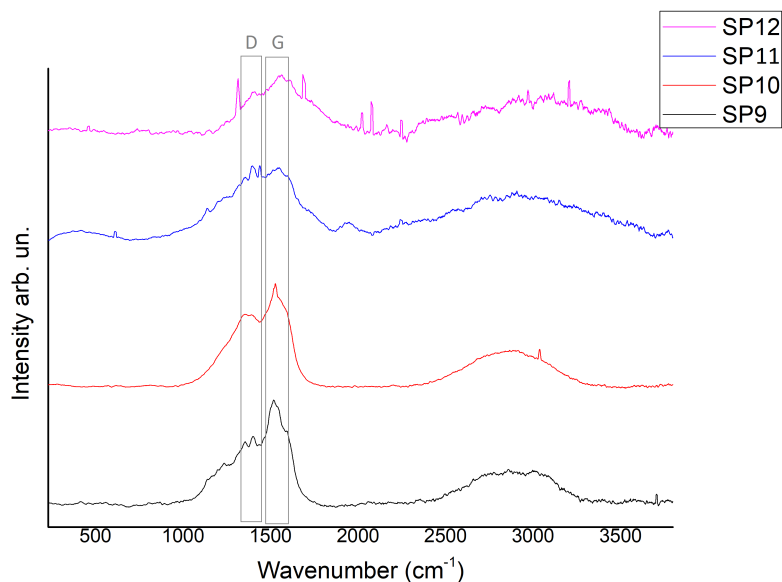


Figure 3.10: Raman spectra of dialyzed C-Dots: SP9 dialyzed, SP10 thermally treated at 250°C and dialyzed, SP11 dialyzed with PEG, SP12 thermally treated at 250°C with PEG and dialyzed.

The Raman spectra observed for dialyzed C-Dots present, as can be seen from figure 3.10 above, more ordered and compact aromatic structure. There are a significant decrease of number of peaks representing functional groups and two bands, D and G, can be easily identified and high ratio between supposed D and G peaks intensity suggests more ordered structure. This confirm the effect of dialysis on the C-Dots, discussed previously.

3.1.3 Absorbance UV/VIS

All C-Dots that shown better performances and then implemented in conjugation where analyzed to obtain an absorption spectrum. The incident radiation scanned from 800nm to 380nm. The C-Dots absorption mechanism was treated in detail in the first chapter. The following results in figure 3.11 are obtained for several samples of thermally treated and dialyzed C-Dots.

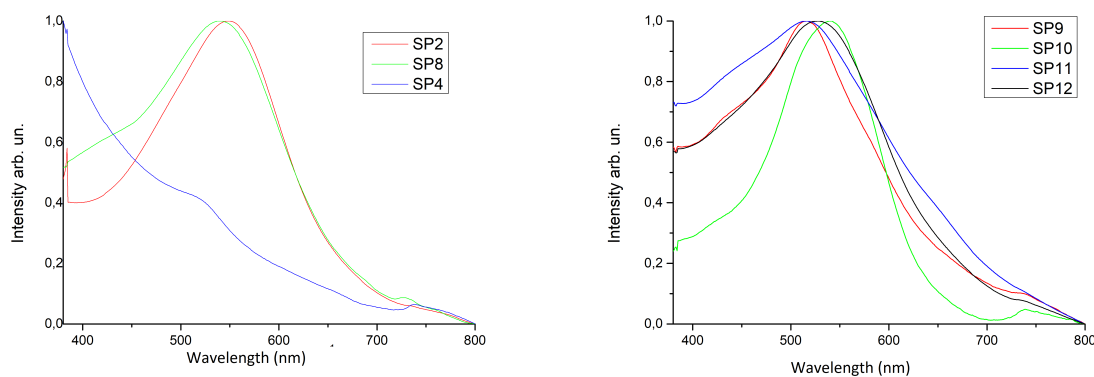


Figure 3.11: Absorption UV/VIS spectrum of SP2 C-Dots thermally treated at 250°C, SP4 C-Dots thermally treated at 450°C and SP8 C-Dots thermally treated at 250°C with PEG-4000 (0.5:1 to CA) (left), SP9 dialyzed C-Dots, SP10 dialyzed C-Dots thermally treated at 250°C and SP11 dialyzed C-Dots with PEG-4000 (0.5:1 to CA), SP12 thermally treated at 250°C (left).

Peaks presented in this wavelength range, above 400nm, are commonly attributed to the presence of N atoms inside the heterocyclic structure of C-Dots. It can be noticed that this band disappears for C-Dots with annealing temperature of 450°C, since thermal treatment promotes the amidation and aromatization changing the C-Dots structure and bonds, as discussed previously. Formation, in this sample, of an increasing trend toward 300-400nm may be attributed to the $n - \pi^*$ transition of C=O or C=N bonds. So, it can refer to the creation of secondary and tertiary amines.

3.1.4 Fluorometer analysis

Again, a set of more performing C-Dots was analyzed with the fluorometer in order to obtain their complete characterization. Fluorometer analyzes were performed with excitation energies from 275nm (4.5eV) to 525nm (2.36eV) and the emission spectra were collected. The following figures 3.12, 3.13 and 3.14 report C-Dots thermally treated at 250°C, at 450°C and at 250°C with PEG-4000 (0.5:1 to CA).

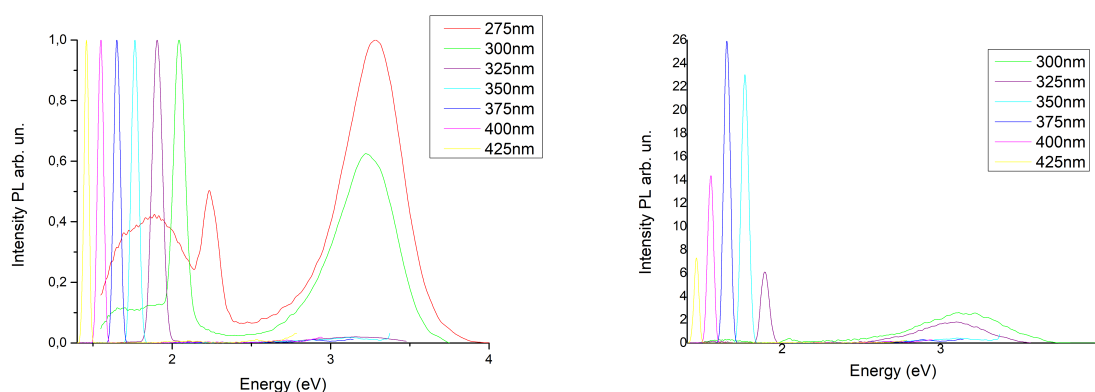


Figure 3.12: Photoluminescence spectra of C-Dots thermally treated at 250°C normalized (right) and not (left).

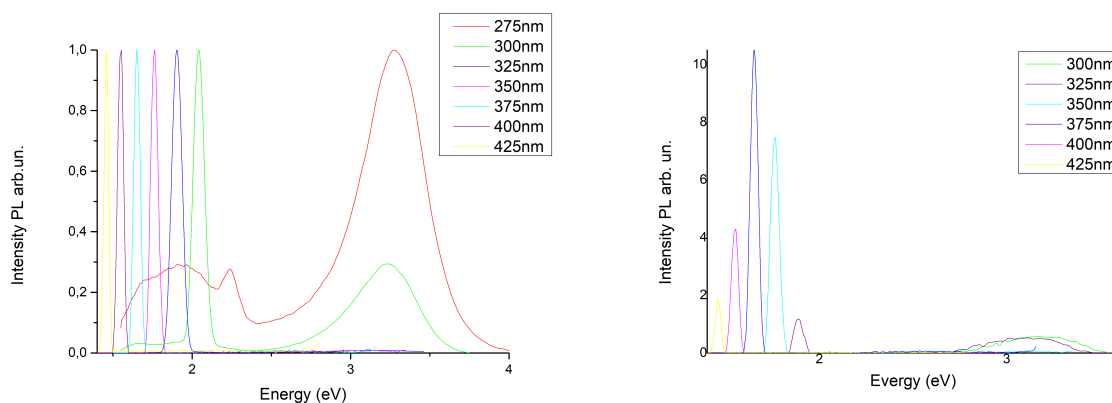


Figure 3.13: Photoluminescence spectra of C-Dots thermally treated at 450°C normalized (left) and not (right).

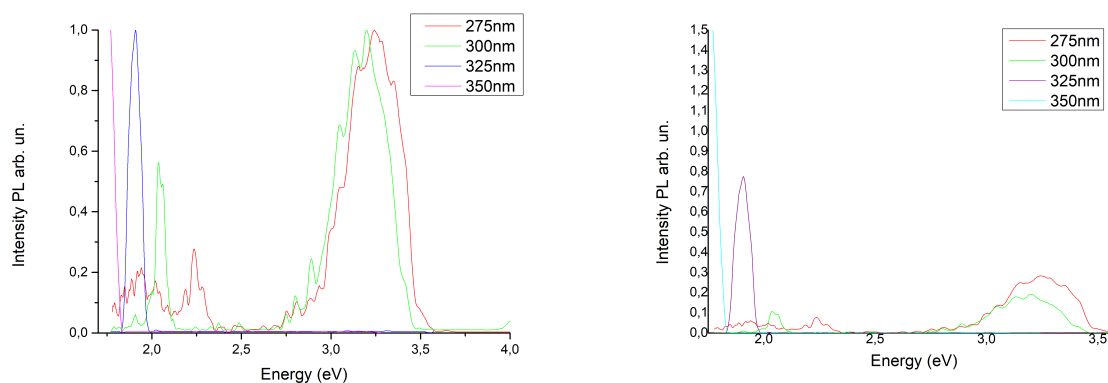


Figure 3.14: Photoluminescence spectra of C-Dots thermally treated at 250°C with PEG-400 (0.5:1 to CA) normalized (right) and not (left).

Analyzing the spectra it is possible to distinguish two types of emission mechanisms in all three samples: excitation dependent and independent. Excitation independent mechanism is characterized by the overlapped bands, which emission energy is the same for different excitation wavelengths. These band can be found in three samples at 1.7-2 eV and 3.2 eV approximately (highlighted on the graphs). They have relatively high energy and are attributed to the $\pi - \pi^*$ transition of the C-Dots graphitic like core. This transition state is also known as HOMO-LUMO gap transition. Furthermore, from the figures arise that, annealing temperatures influence bands relative intensity. This is related to the fact that thermal treatment promotes the C-Dots carbonization and condensation. So, intensity variation may be related to the structural change inside the C-Dots core, as it dependence on size and edge states. When the later size of C-Dots increases their band gap decreases changing the transition states, as discussed in previous chapter.

Comparing C-Dots treated at 250°C with and without PEG-4000, quantum yielding variations are noticeable. In this case also excitation dependent bands are changed. Excitation dependent bands present at lower energies can be related to $n - \pi^*$ inside band transitions. The emission occurs at lower energies due to the creation of energy levels inside HOMO-LUMO band related to different functional groups. In this case PEG-4000 might introduce some functionalizations and direct the C-Dots condensation since, both emission dependent and not bands changes intensity.

However, since the C-Dots internal structure is difficultly defined, these emission bands attribution has no certainty.

Also dialyzed C-Dots with and without PEG-4000 (0.5:1 to CA) were analyzed and reported in figures 3.15 and 3.16:

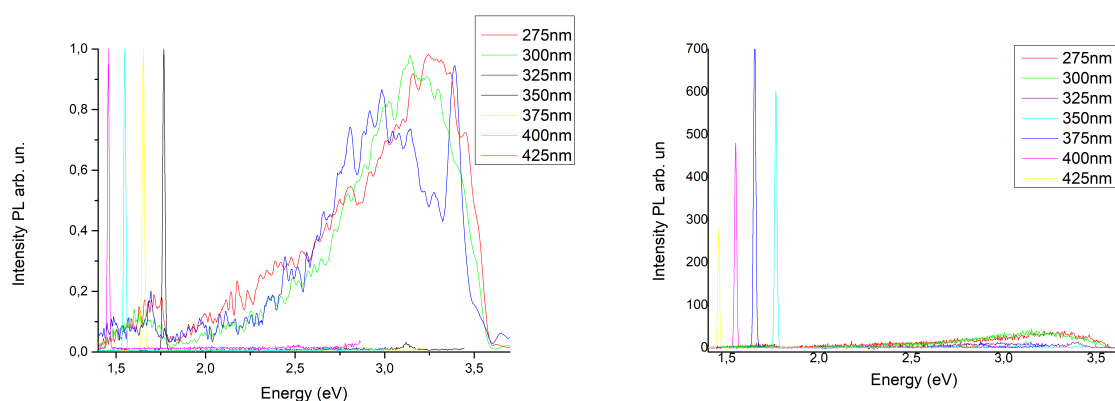


Figure 3.15: Photoluminescence spectra of dialyzed C-Dots normalized (left) and not (right).

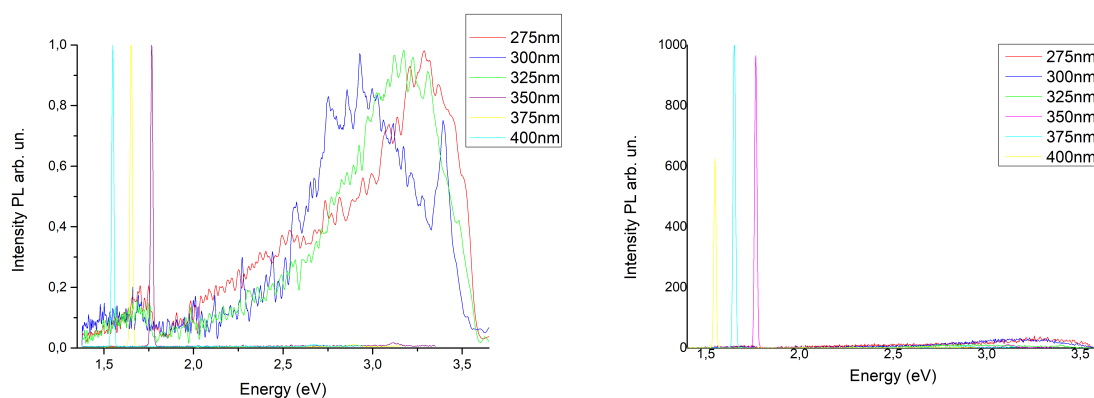


Figure 3.16: Photoluminescence spectra of dialyzed C-Dots with PEG-4000 normalized (left) and not (right).

For dialyzed C-Dots the excitation independent band is large and composed by overlapping of several peaks, probably related to different core energy levels of more ordered purified C-Dots.

Furthermore, from not normalized spectra of all analyzed samples it was observed that the excitation independent bands present low signal/noise ratio and they are much less intense with respect to excitation dependent bands. So as expected, the quantum yielding is higher for excitation dependent band related to the C-Dots surface functionalization.

3.2 Bismuth Oxide based microparticles

Bismuth oxide particles produced through hydrothermal method have an advantage of lower synthesis temperature with respect to the solid state one (80° respect to 450° and 550°). Its chemical reaction is reported in figure 3.17.

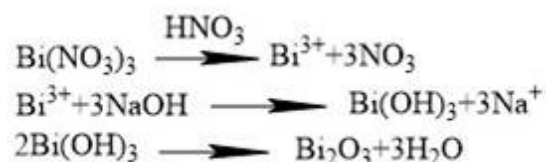


Figure 3.17: Bismuth Oxide hydrothermal chemical reaction.

Due to the low water solubility of the Bismuth Nitrate pentahydrate, its solution is done in acidic environment generated by adding some drops of Nitric Acid. When the precursor is completely dissolved in water, Sodium Hydroxide is added at room temperature, because the reaction could be exothermic and solution reaches approximately 10pH forming Bismuth Hydroxide, which is extremely unstable. Solution pH can modify the growth mechanism, so it is possible to change the NaOH concentration in order to obtain different crystal morphologies [92]. At the end of reaction, Bismuth Hydroxide decomposes itself forming a yellow precipitate of Bismuth Oxide. In order to change the characteristics and performances of microparticles, four different active surfactants that direct the synthesis are added. They are physically absorbed on the microparticles surfaces and can favour a growth and a subsequent conjugation. Two types of active surfactants are analyzed: ionic and non-ionic active surfactants. Also the effect on growth mechanism of active surfactant concentration was tested with two different concentrations of PEG-4000.

Ionic surfactants dissociate into water and expose the polar heads towards the aqueous phase, Lauric Acid and Sodium Lauryl Sulphate are considered.

Non-ionic surfactants present helical chain with alternating hydrophobic and hydrophilic parts. They don't dissociate and perform their function through the steric hindrance tending to arrange their hydrophilic parts toward aqueous phase, in this case polyethylene glycol and polyvinylpyrrolidone are used.

These active surfactants are added after the Bismuth Hydroxide formation. The growth mechanism is layer-by-layer and it is discussed by Wang and Li in their work [92] and reported in figure 3.18.

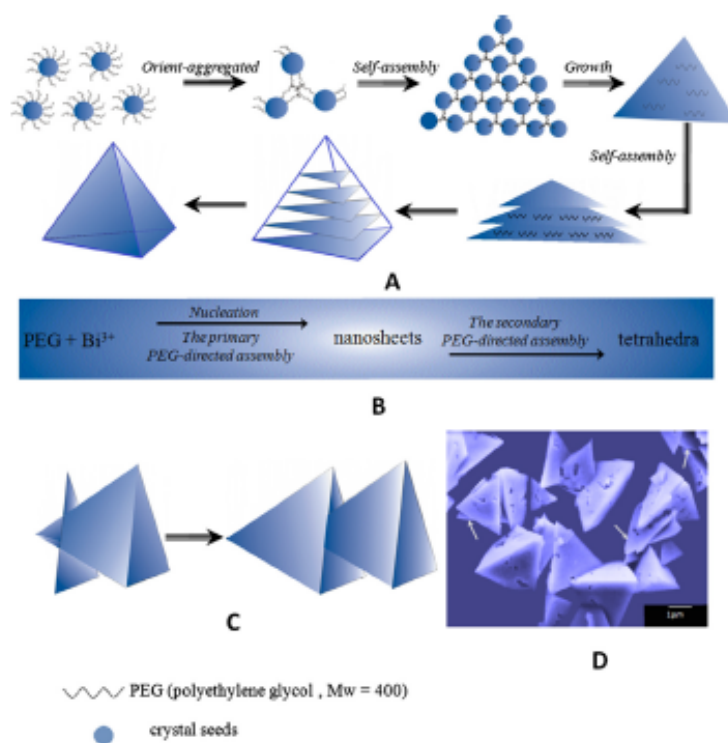


Figure 3.18: Schematic illustration of a growth self assembling mechanism of Bismuth Oxide microparticles [92].

Tetrahedral structures are formed layer-by-layer through self-assembling mechanism directed by active surfactants, which play a crucial role in the final morphology of these reactions. These, besides the fact that they reduce the dimensions and avoid the aggregation between microparticles by means of the micelle or liposome formation (figure 3.19), direct and join colloidal Bi_2O_3 nanoparticles in the triangular layers thanks to their hydrophilic and hydrophobic parts. In this way, the active surfactants direct also the following gradually smaller nanosheets to the parallel formation with respect to the first one seed layer. Moreover, it is possible that a new seed layer forms in another direction to the previous one, so the cross-linked structures can grow.

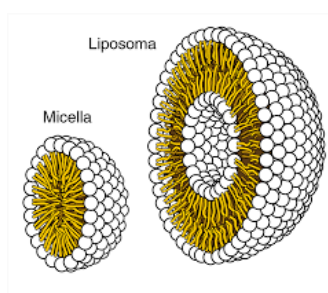


Figure 3.19: Schematic representation of micella and liposoma formation through an ionic surfactant.

Also the solid state syntheses are performed starting from Bismuth Nitrate pentahydrate without additional solvents. Controlled thermal decomposition is carried out using gradually increased calcination temperatures in a gradual way, obtaining the polymorphous heterostructures containing Bi_2O_3 and $Bi_5O_7NO_3$. Decomposition mechanism is responsible of the morphology, porosity and composition of the final product and it can be controlled by different set of calcination temperatures, time of reaction and cooling proceeding [93]. With increasing temperature $Bi_5O_7NO_3$ phase is formed and undergo a gradual expulsion of volatile substances. At high enough temperature Bi_2O_3 starts to form and a heterostructure is created. In order to have a total conversion in Bi_2O_3 a high threshold temperature must be reached for a sufficiently long time. Due to the high porosity of this heterostructure its surface area is quite large and is predisposed to contain several functional groups and surface contaminations.

3.2.1 FESEM

The hydrothermally obtained Bismuth Oxide particles morphology was analyzed by FESEM. From these analyses arised that the particles synthesized in this way are of micrometric dimensions, this, as explained previously, can be an advantage in the in-vivo applications. Furthermore, from FESEM imagines in figure 3.20 and figure 3.21, it was observed that the particles synthesized without any active surfactants present irregular structure growth with different shapes and many particles are aggregated. There are breaks due to the planes that grow into a castle of paper and collapse. The planes grow is complicated and there is not preferential morphology and direction.

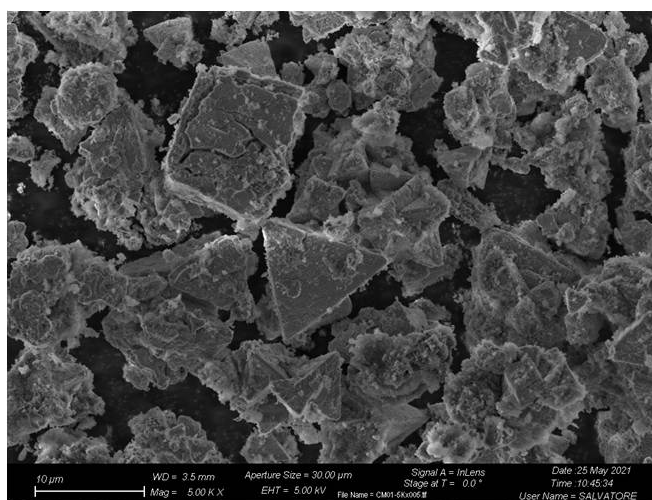


Figure 3.20: FESEM imagine of Bismuth Oxide without active surfactant.

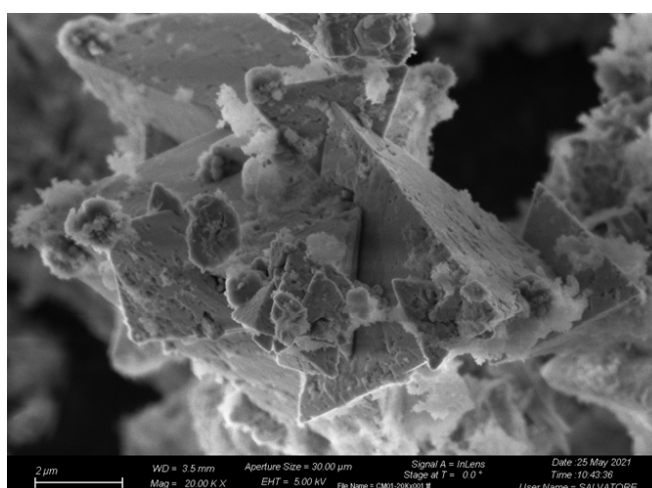


Figure 3.21: FESEM imagine of Bismuth Oxide without active surfactant.

The most regular growth were obtained adding PEG-0400 (figure 3.22 and figure 3.23) and SLS (figure 3.24) as active surfactants (non-ionic and ionic respectively), the structures are organized in tetrahedrally shaped structures and sometimes cross-linked. So, these active surfactants have been decomposed in the solution forming micelles and interacting with the particles themselves, and due to their chain structure configuration, confine the formation rate of crystal faces which causes an anisotropic growth.

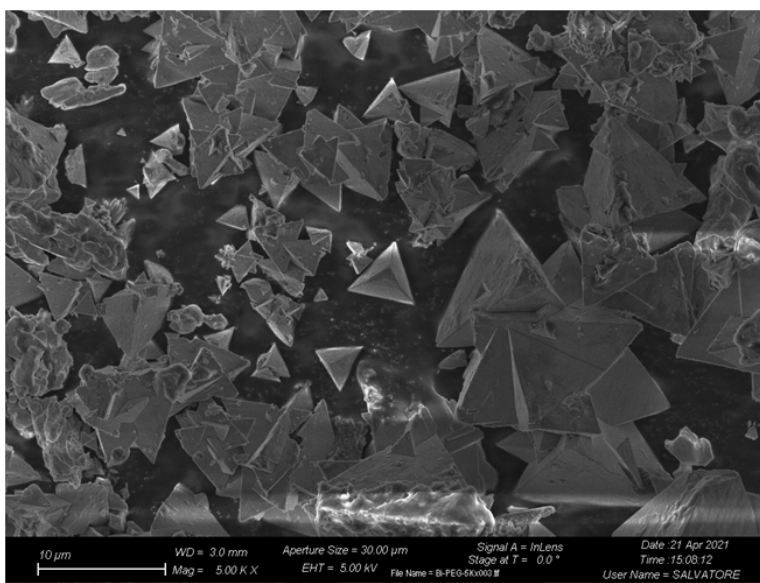


Figure 3.22: FESEM image of Bismuth Oxide with PEG.

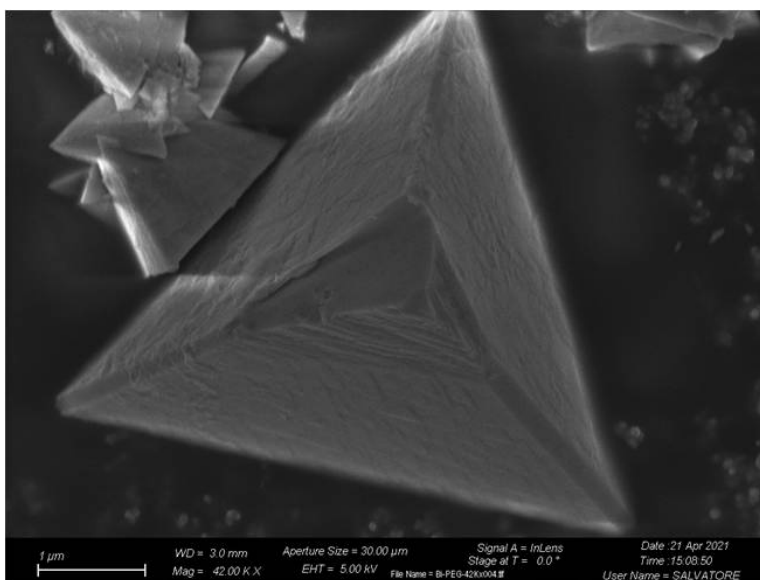


Figure 3.23: FESEM image of Bismuth Oxide with PEG.

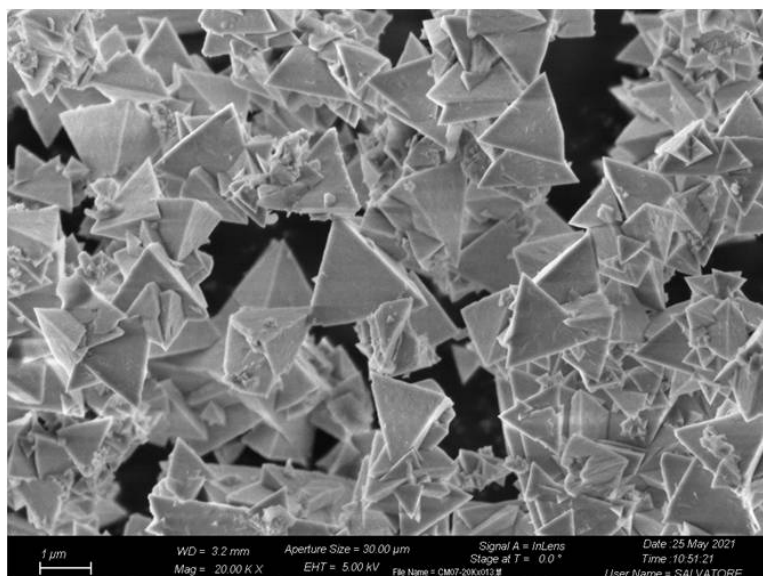


Figure 3.24: FESEM image of Bismuth Oxide with SLS.

The situation is different for PVP (figure 3.25) and LA (figures 3.26 and 3.27). Their morphology is irregular, disordered and without preferential planes of growth. Although, in the case of PVP it is possible to notice some hints of tetrahedral structures, in the sample synthesized with LA there are aggregations and several geometrical shapes with no one predominant. This can be explained by the fact that maybe these active surfactants have not dissolved in a basic environment (LA case), or only partially dissolved (PVP case), and have not formed micelles or liposomes so, consequently they have not performed their direction function.

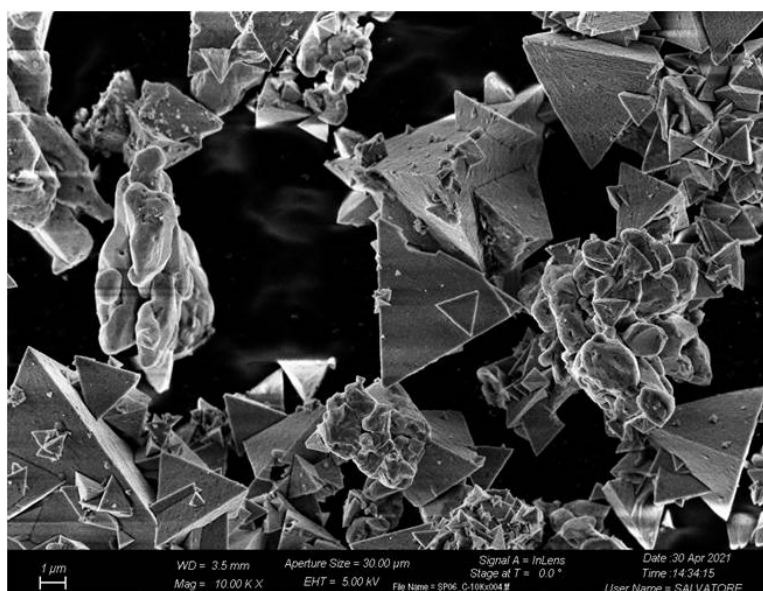


Figure 3.25: FESEM image of Bismuth Oxide with PVP.

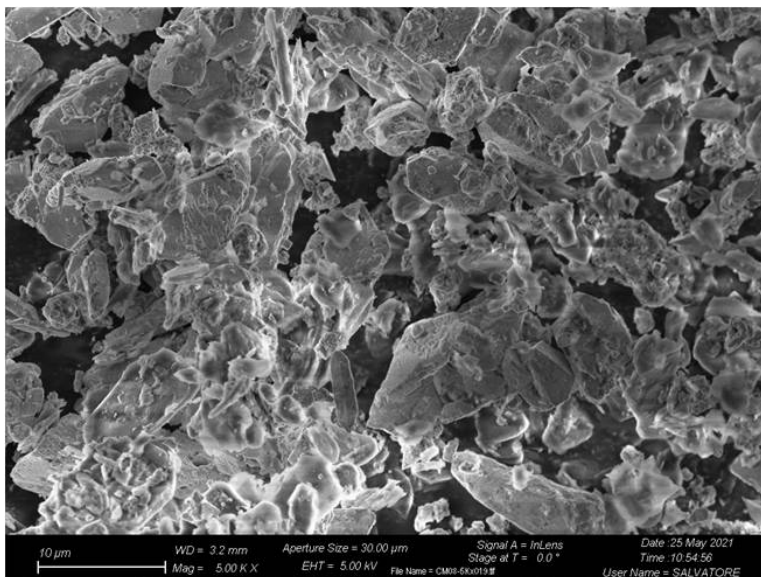


Figure 3.26: FESEM imagine of Bismuth Oxide with LA.

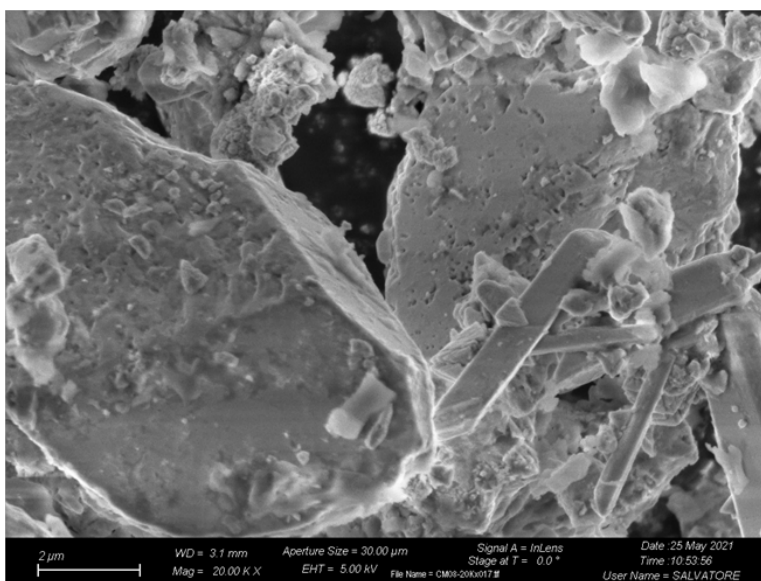


Figure 3.27: FESEM imagine of Bismuth Oxide with LA.

In order to test the growth mechanism dependence on the amount of an active surfactant, the synthesis was repeated adding a double amount of PEG-4000, which gave a more regular structure. From figures 3.28, 3.29 and 3.30 it is possible to notice that there is a slight decrease of the average particles dimensions with good morphological and better, with respect to the case of 5% wt. PEG-4000, size homogeneity.

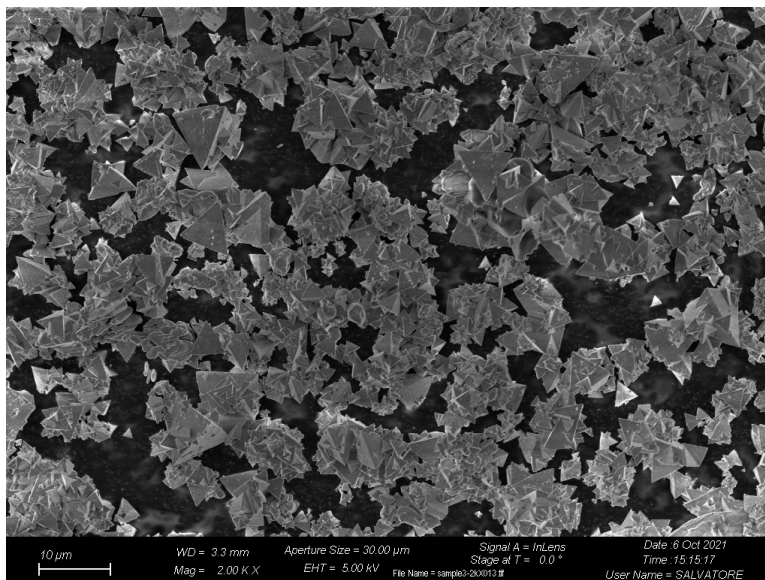


Figure 3.28: FESEM imagine of Bismuth Oxide with PEG 10%wt.

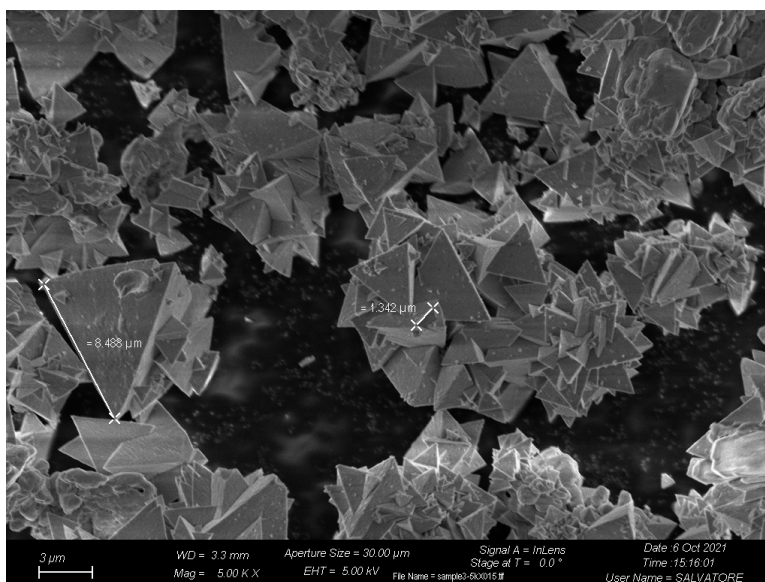


Figure 3.29: FESEM imagine of Bismuth Oxide with PEG 10%wt.

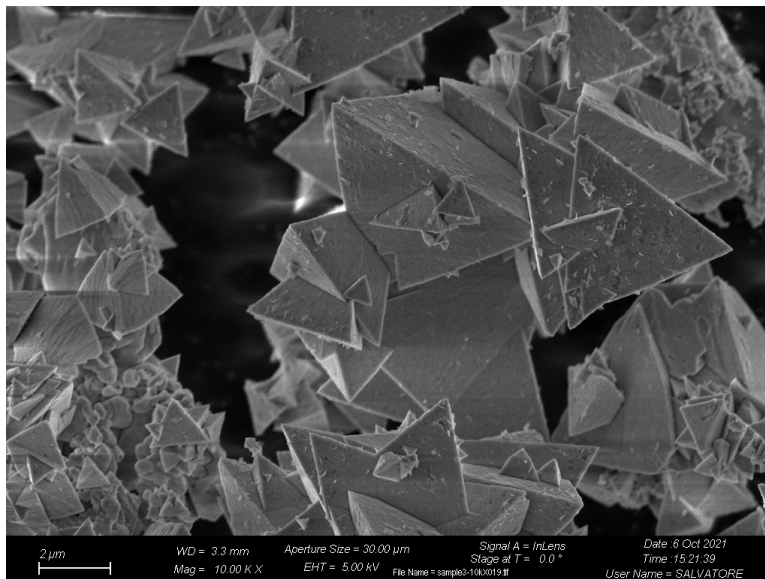


Figure 3.30: FESEM image of Bismuth Oxide with PEG double amount.

FESEM images reported in following figures 3.31, 3.32 and 3.33 were created from solid state synthesized microparticles containing Bi_2O_3 and $Bi_5O_7NO_3$. As expected, these particles present very irregular morphology with high concentration of nanoshaped porosity sites.

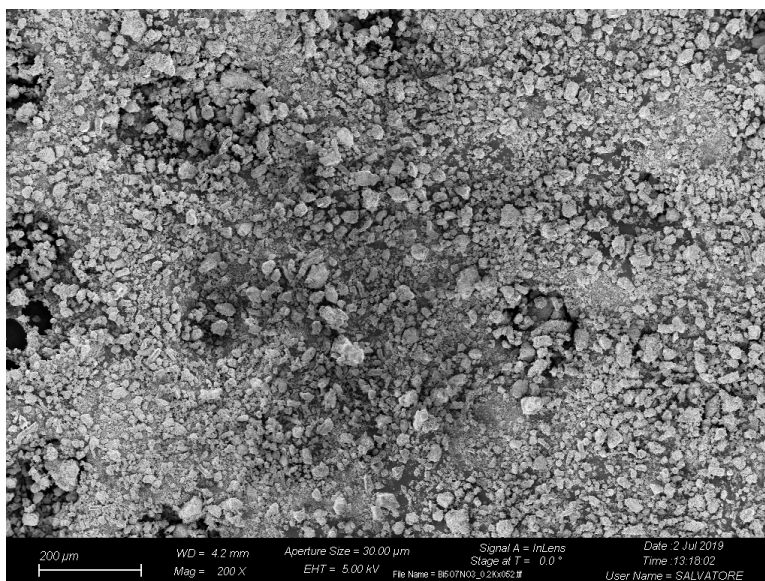


Figure 3.31: FESEM image of Bismuth Oxide based nanoparticles synthesized with solid state procedure.

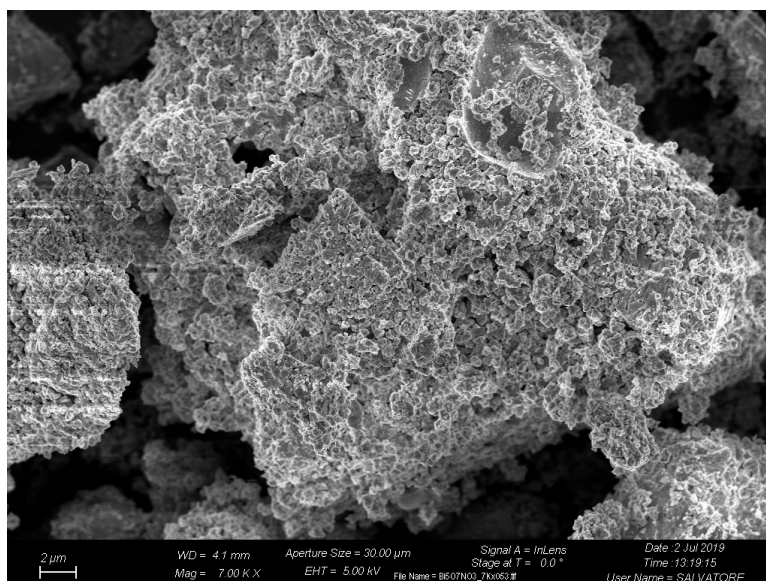


Figure 3.32: FESEM image of Bismuth Oxide based nanoparticles synthesized with solid state procedure.

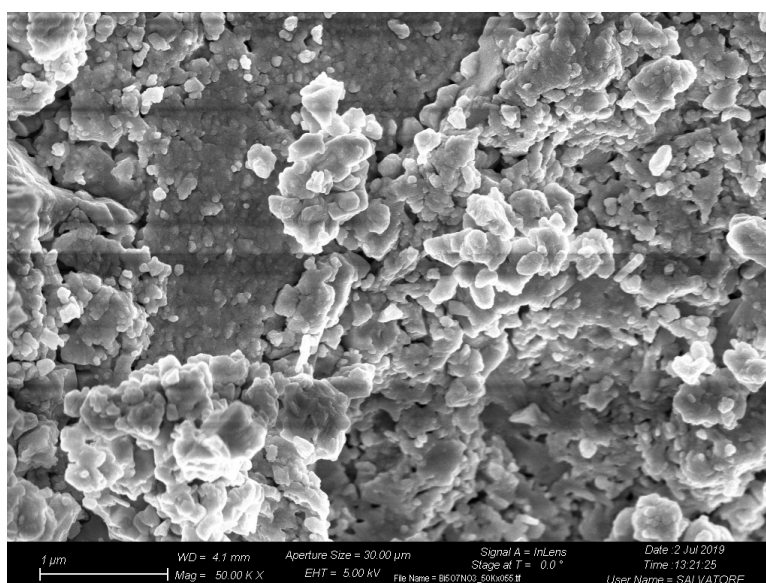


Figure 3.33: FESEM image of Bismuth Oxide based nanoparticles synthesized with solid state procedure.

3.2.2 Raman spectroscopy

Raman spectroscopy was used to investigate the samples core and surface structure. Analyzing the spectrum of hydrothermally obtained Bismuth Oxide microparticles and comparing it with that of the Bismuth Nitrate pentahydrate used as reagent (3.34), it is evident that the characteristic Bismuth Nitrate peak indicating ν_s (approximately 1050cm^{-1}) and the ν_{as} band (near 1500cm^{-1}) of NO_3^- disappears, suggesting that the reaction is occurred completely. Furthermore, bellow 500cm^{-1} it is possible to individuate typical Bismuth Oxide peaks originated from the ν_{B-O} . So, it confirms that the Bismuth Oxide synthesis reaction is has been completed.

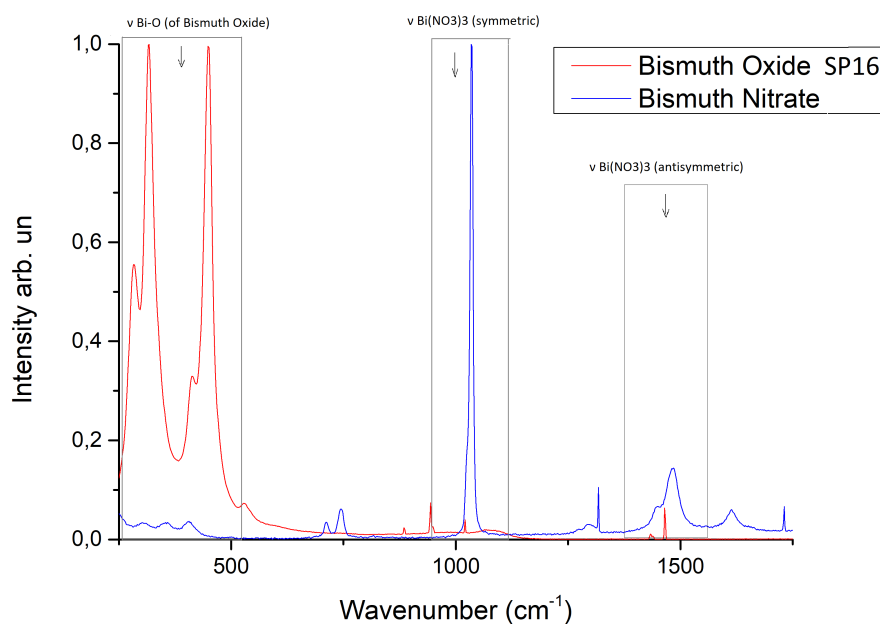


Figure 3.34: Comparison between obtained used Bismuth Nitrate and Bismuth Oxide.

Comparing microparticles synthesized with different active surfactants in figure 3.35, they present ν_{B-O} peaks with different proportions one to each other due to different effects active surfactant have on the structure morphology. Also from Raman spectrum it can be noticed that PVP has produced a highly defected structure with respect to the others.

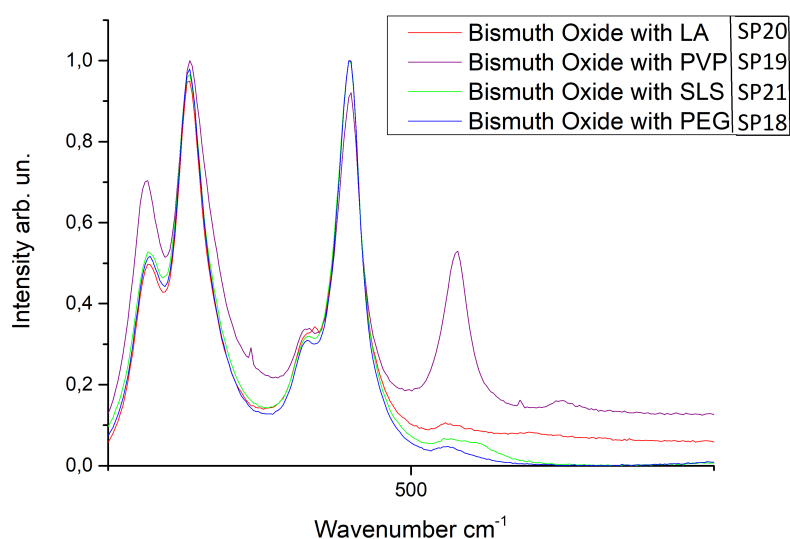


Figure 3.35: Comparison between Bismuth oxide microparticles with different active surfactant: LA, PVP, SLS, PEG.

Regarding the particles obtained with solid state procedure (figure 3.36), their Raman spectrum still contains the typical Bismuth Nitrate peak, so, as was supposed, the conversion in Bismuth Oxide is only partial. Analyzing the same sample in different points, it is evident that the peaks are not all the same because this is an intermediate level, where the structure is extremely heterogeneous.

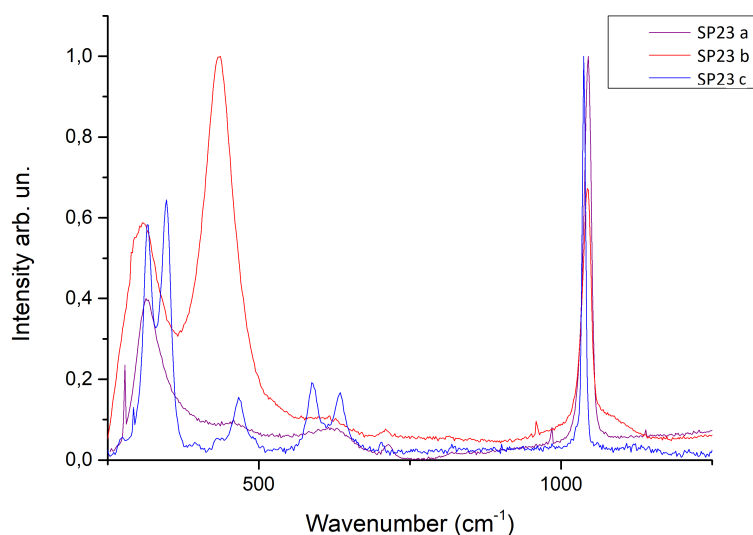


Figure 3.36: Raman spectra of solid state Bismuth Oxide based microparticles analyzed in different points and different syntheses.

3.3 Conjugations

The most promising and interesting samples of C-Dots were combined with that of Bismuth Oxide microparticles in order to have a complete overview of several possible conjugation and examine their grade of interaction. Samples implemented in this part of work were: SP2, SP4, SP7, SP8, SP9, SP10, SP11, SP12 for C-Dots and SP23, SP18, SPSP22 for nanoparticles.

The conjugation interaction is of an electrostatic nature, and occurs through the weak interactions of H-bonding and back-bonding. The former is explained by -OH groups present on microparticles surface, due to numerous defects, with O and N atoms on the C-Dots surface. The later is due to the presence of π orbitals of the C-Dots, generated from their aromatic structure, and d orbitals present on the metallic microparticles surfaces. Also the common weak interaction can occurs between these particles, as those of Van der Waals, dipole-dipole and others. After the separation by centrifugation, residual and soluble part of the conjugation reaction are submitted to some analysis in order to have a confirm of the successful .

3.3.1 FESEM

FESEM was implemented to analyze the morphology of the most regular sample of the hydrothermal Bismuth Oxide microparticles, that is the one containing PEG-4000 (5% of Bismuth mass), and dialyzed C-Dots that shows a great purification effects. From figures 3.37, 3.38 and 3.39 it is possible to see that C-dots have covered the Bismuth Oxide microparticles surface, suggesting the conjugation. More precisely, dialyzed C-Dots did not simply cover the microparticle surface, but promoted also exfoliation of the planes which create their tetrahedral structure, as discussed previously.

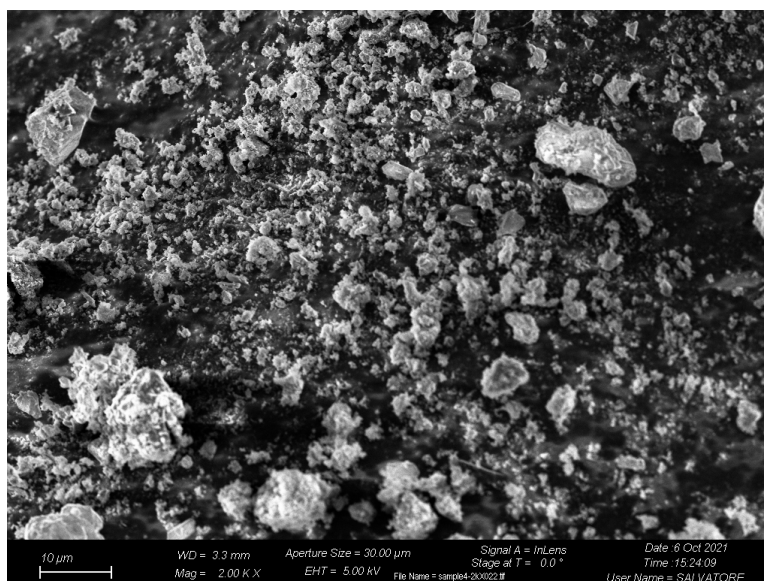


Figure 3.37: FESEM spectrum of conjugation SP33: hydrothermal Bismuth Oxide microparticles with PEG-4000 and dialyzed C-Dots.

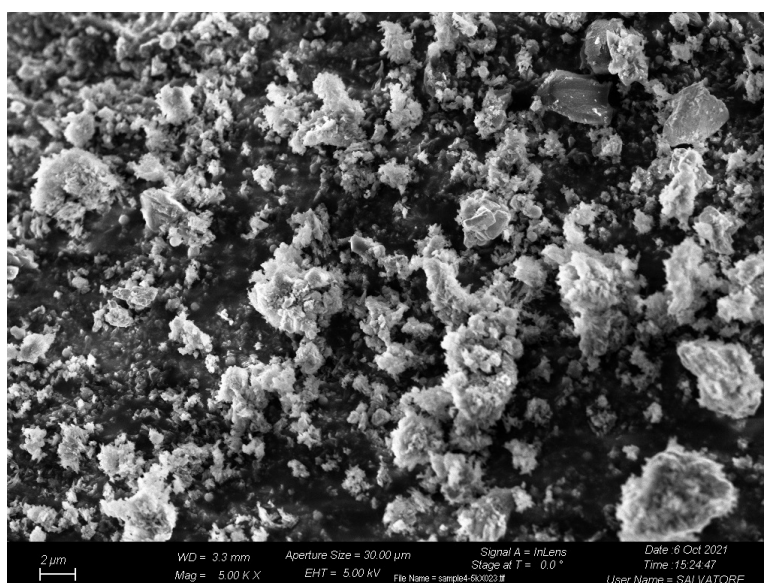


Figure 3.38: FESEM spectrum of conjugation SP33: hydrothermal Bismuth Oxide microparticles with PEG-4000 and dialyzed C-Dots.

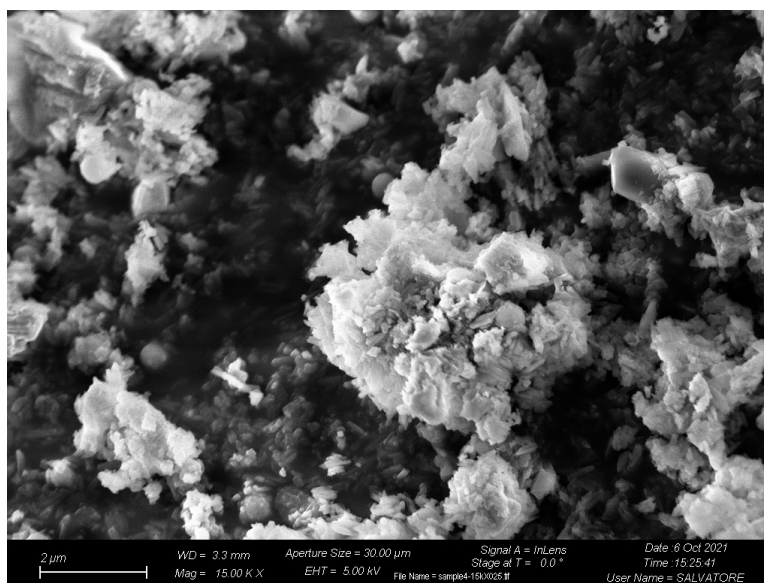


Figure 3.39: FESEM spectrum of conjugation SP33: hydrothermal Bismuth Oxide microparticles with PEG-4000 and dialyzed C-Dots.

3.3.2 FT-IR spectroscopy

IR spectra of all conjugations are analyzed and compared.

IR spectra of Solis State particles conjugated with thermally treated C-Dots with and without PEG-4000 are reported below in figures 3.40 and 3.41. For these samples, both residual and soluble parts are analyzed in order to have a confirm of the occurred conjugation. For better comparison also IR spectrum of used C-Dots is reported.

The interaction with molecules of Bismuth Oxide stiffens the structure and changes the vibrational modes of the C-Dots. In both, residue and solution, the band related to skeletal vibrations is inhibited indicating the greater strength and rigidity of the structures. Regarding mainly the residue spectra, the band due to unsaturated ν_{C-H} is inhibited due to the $\pi - d$ interaction with the microparticles surface. Here also $\nu_{C=C}$ decreases in intensity with respect to the C-Dots and conjugation soluble part due to the inhibition of the ring vibration as a consequence of interactions. Also the peaks related to the C-Dots functional groups are inhibited after interaction and change their relative intensities. So, there are many aspects indicating that the conjugation occurred successfully in the residue.

Figure 3.40 show the conjugations of particles synthesized through solid state method with C-Dots thermally treated at 250°C and 450°C respectively:

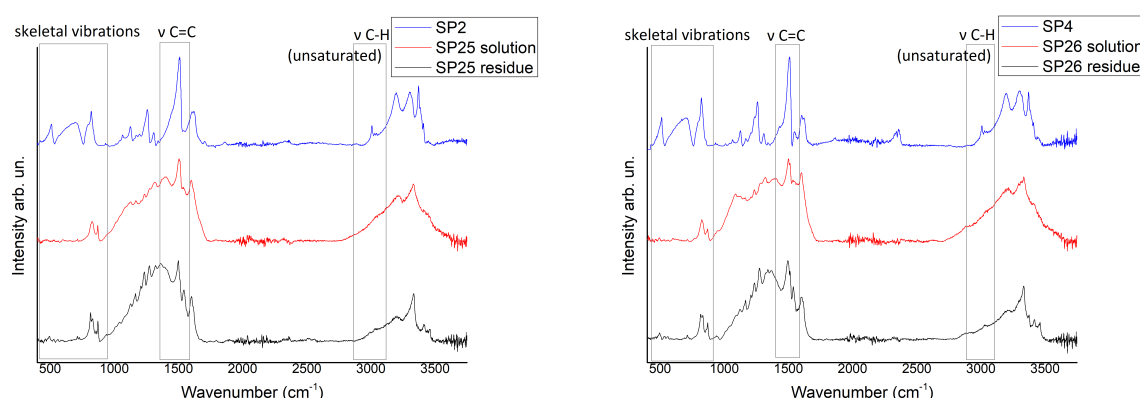


Figure 3.40: IR spectra of SP25 (left) SP26 (right) conjugations residue, solution and their C-dots

From the spectrum of conjugations with thermally treated (250°C) C-Dots containing PEG-4000 (figure 3.41 0.1:1 and 0.5:1 to CA respectively) it can be notice that, since, as discussed before, PEG-4000 promotes the conjugation with particles, the inhibition of the residue $\nu_{C=C}$ is further more evident.

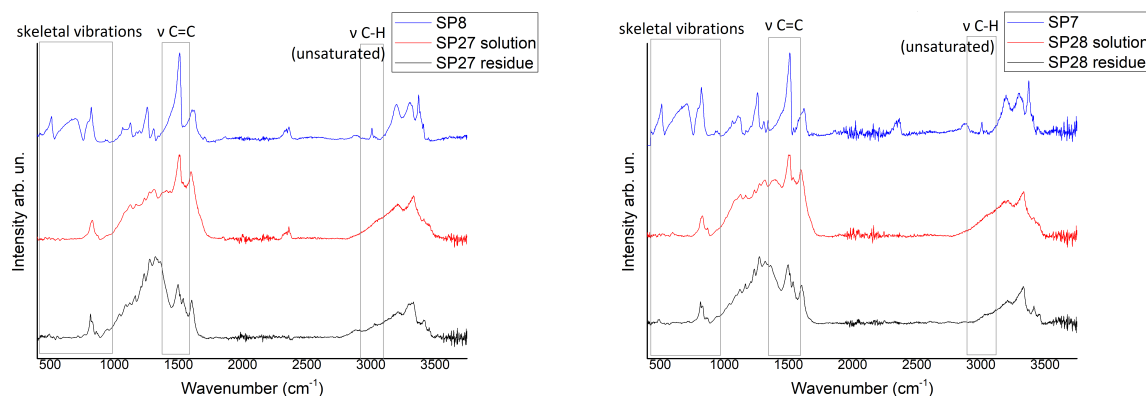


Figure 3.41: IR spectra of SP27 (left) SP28 (right) conjugations residue, solution and their C-dots

From now on, only the residue is analyzed, since the hypothesis that it contains majority of conjugations is confirmed.

Also the thermally synthesized microparticles of Bismuth Oxide with PEG-4000 active surfactant conjugated with thermally treated C-Dots at 250°C with and without PEG-4000 (0.1:1 and 0.5:1 to CA) are analyzed through IR spectroscopy in figure 3.42 respectively. The observations made for the previous conjugation are valid also in these cases.

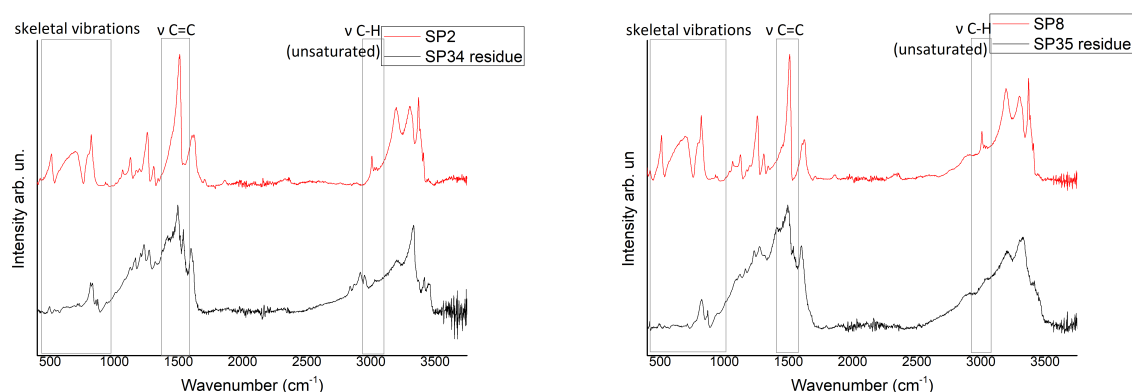


Figure 3.42: IR spectra of SP34 (left) SP35 (right) conjugations residue and their C-dots

To have a complete set of analyzes, also the conjugation containing thermally treated C-Dots with PEG-4000 (0.5:1 o AC) and microparticles with double amount of PEG-4000 active surfactant and the direct one conjugation were analyzed in figure 3.43. A slight difference can be noticed figure for the direct conjugation (3.43 (right)), but a certainty of conjugation comes from skeletal vibration band and from $\nu_{C=C}$ and unsturated ν_{C-H} inhibition that, just like in previous cases, indicates the formation of weak interaction of $\pi - d$ type between C-Dots and forming microparticles surfaces during the synthesis.

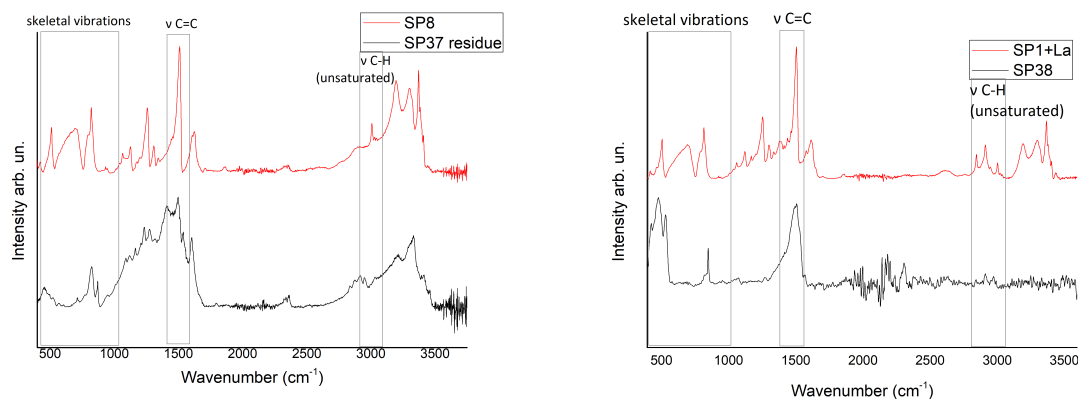


Figure 3.43: IR spectra of SP37 (left) and SP38 (right) conjugations residue and their C-dots

Now, the conjugations using a set of thermally treated with and without PEG-4000 (0.5:1 to AC) dialyzed C-Dots are reported and analyzed. Hydrothermally synthesized Bismuth Oxide microparticles with PEG-4000 surfactant and subsequently conjugated with dialyzed C-Dots (figure 3.44 (left)), thermally treated at 250°C dialyzed C-Dots (figure 3.44 (right)), dialyzed C-Dots with PEG-4000 (figure 3.45 (left)) and thermally treated at 250°C dialyzed C-Dots with PEG-4000 (figure 3.45 (right)) present the following IR spectra. As discussed previously, dialyzed C-Dots, due to their rigidity, have inhibited skeletal vibration band with respect to the thermally treated C-Dots. So, conjugation can be observed from the decreased $\nu_{C=C}$ peak due to the weak interaction with Bi_2O_3 microparticles surface.

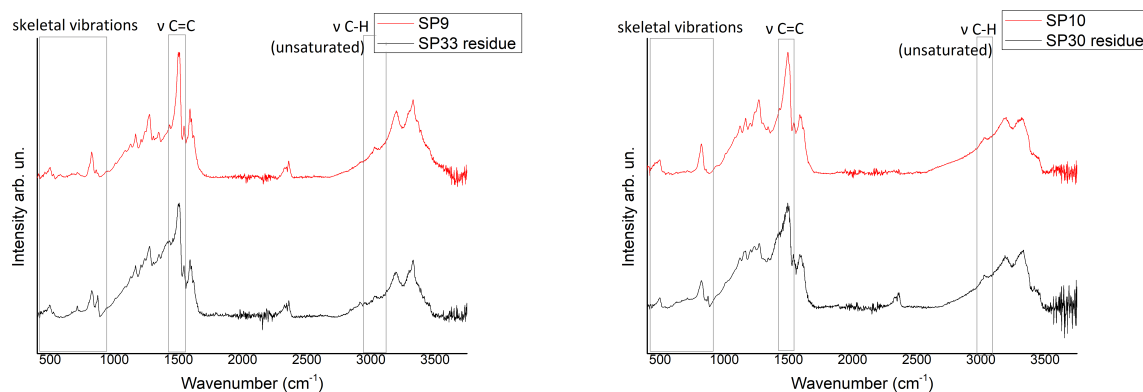


Figure 3.44: IR spectra of SP33 (left) and SP30 (right) conjugations residue and their C-dots

From samples containing dialyzed C-Dots with PEG-4000 it can be seen that a noticeable peak of saturated ν_{C-H} presented in IR spectrum between $2800 - 2950\text{cm}^{-1}$, characteristic of the PEG-4000 presence, disappears. PEG-4000 polymers are physically absorbed on the microparticles and C-Dots surfaces.

When these are put in aqueous phase during, PEG-4000 promotes their conjugation creating a micella around them. At the end of the synthesis, conjugations are created and PEG-4000 is no more present on their surfaces.

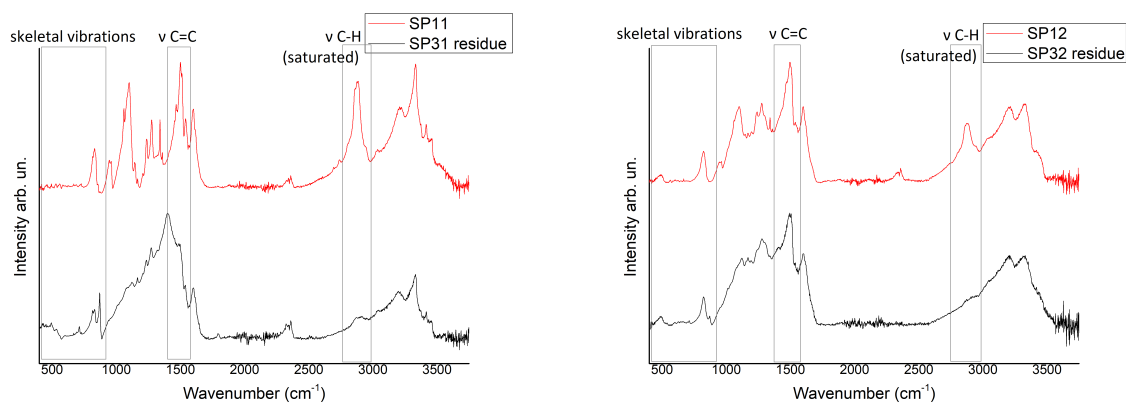


Figure 3.45: IR spectra of SP31 (left) and SP32 (right) conjugations residue and their C-dots

Following graphs (figure 3.46) represent also the conjugations of dialyzed C-Dots with particles synthesized with double amount of PEG-4000 and that through solid state synthesis respectively:

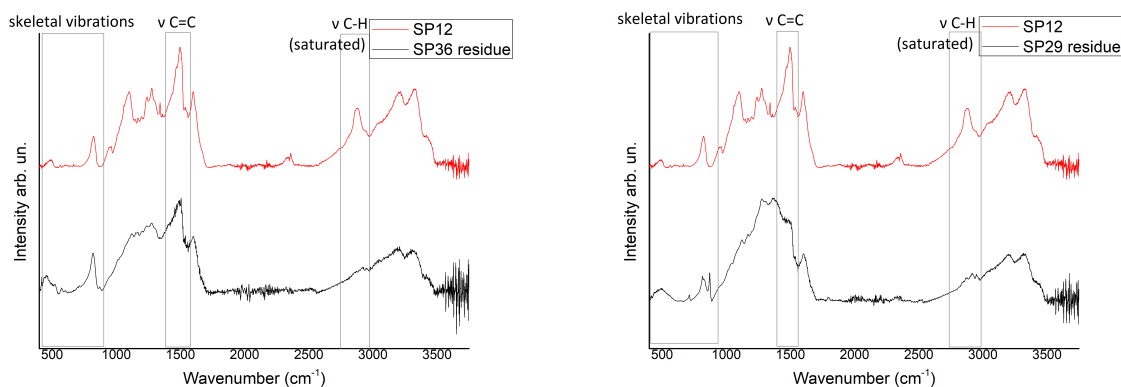


Figure 3.46: IR spectra of SP36 (left) and SP29 (right) conjugations residue and their C-dots

3.3.3 Raman spectroscopy

Similar observations and conclusions can be taken also from the Raman spectra of the synthesized conjugations.

For better comparison, conjugation spectra are reported with their precursors, Bismuth Oxide particles and C-Dots.

Firstly, Raman spectra of solid state synthesized Bismuth Oxide based particles conjugated with C-Dots thermally treated at 250°C (figure 3.47 (left)), 450°C (figure 3.47 (right)) and thermally treated at 250°C with PEG-4000 (0.1:1 (figure 3.48 (left)) and 0.5:1 (figure 3.48(right)) to AC). These conjugations present only aspects related to the C-Dots modes, band between 1000 and 1700 cm^{-1} , this might be due to both the thick layer of C-Dots coverage (at least 1 μm) or inhibition of characteristic Bi_2O_3 modes below 500 cm^{-1} due to the interaction with C-Dots surface. It is possible to notice a change in relative proportions of the bands, suggesting a conjugation due to a variation of the stretching modes of functional groups, however this is not so appreciable like in IR spectra due to C-Dots high fluorescence. Any characteristic peak of Bismuth Oxide or Bismuth Nitrate, it can be deduced that the C-Dots coverage layer is quite thick or the interaction inhibits these bands.

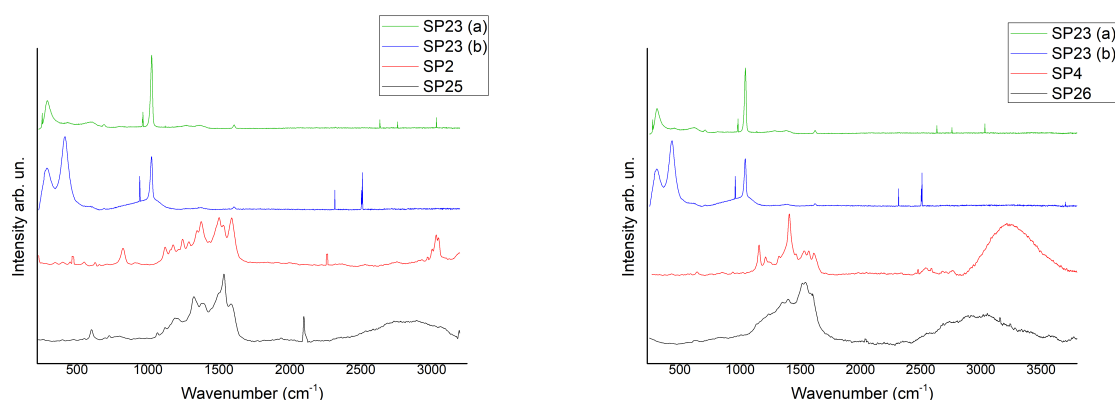


Figure 3.47: Raman spectra of SP25 (left) and SP26 (right) conjugation residue, their C-dots and Bismuth Oxide microparticles

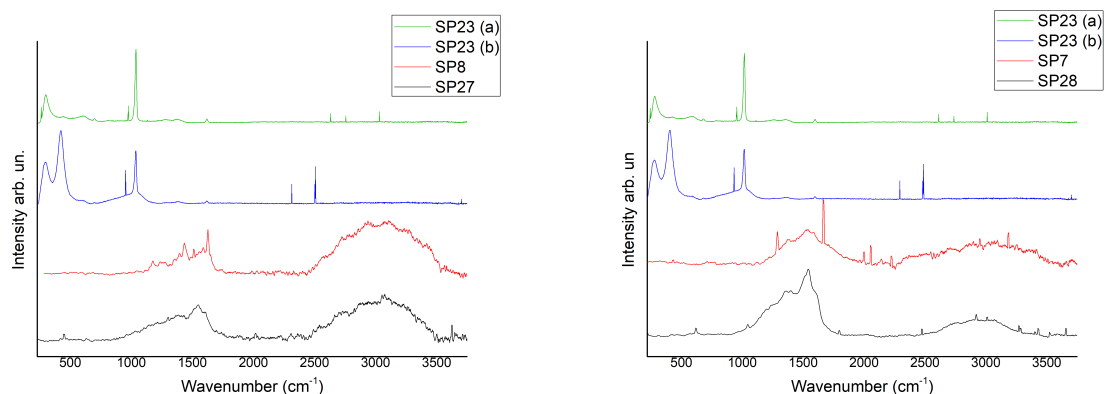


Figure 3.48: Raman spectra of SP27 (left) and SP28 (right) conjugation residue, their C-dots and Bismuth Oxide microparticles

Different behaviour is observed for conjugation that used hydrothermally synthesized Bismuth Oxide microparticles with PEG-4000 surfactant and thermally treated at 250°C C-Dots with (0.5:1 to CA in figure 3.49 (left) and without PEG-4000 in figure 3.49 (right)). In both spectra, especially in the second one which C-Dots present PEG-4000, the conjugations suggest also a presence of Bismuth Oxide microparticles below 500 cm^{-1} , even if these characteristic peaks related to Bismuth Oxide are inhibited and slightly shifted due to interaction effects on these modes. So, different combination of microparticles and C-Dots has different effects on the vibrational modes and/or on the thickness of C-Dots coverage.

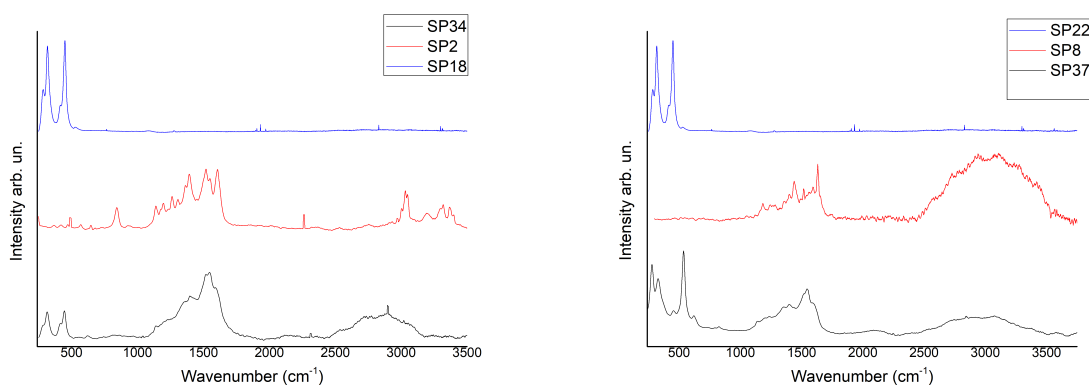


Figure 3.49: Raman spectra of SP34 (left) and SP37 (right) conjugation residue, their C-dots and Bismuth Oxide microparticles

Analyzing hydrothermally prepared Bismuth Oxide microparticles conjugated with dialyzed C-Dots in figure 3.50 (left) and thermally treated at 250°C dialyzed C-Dots in figure 3.50 (right), Their Raman spectra remind those of used C-Dots and there are no characteristic peaks related to the Bismuth Oxide modes. Changes of peaks related to the dialyzed C-Dots functional groups modes are

minimal, because dialyzed C-Dots present extremely low functionalization with respect to that thermally treated.

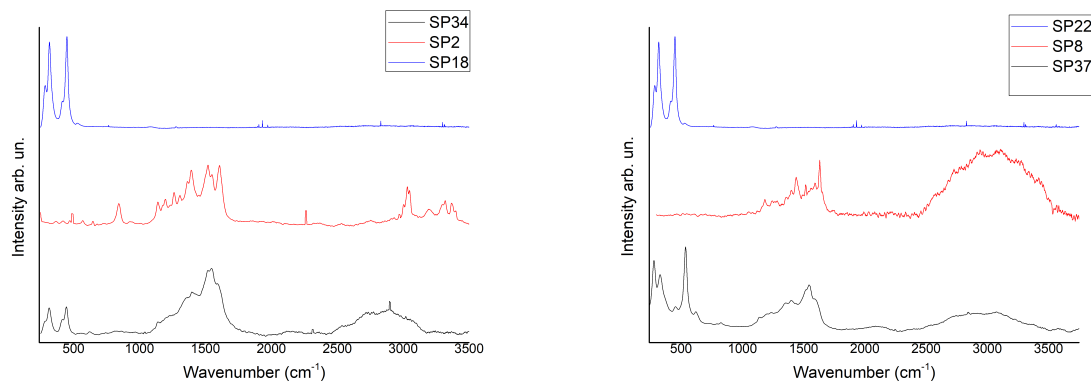


Figure 3.50: Raman spectra of SP34 (left) and SP37 (right) conjugation residue, their C-dots and Bismuth Oxide microparticles

Instead, the PEG-4000 (0.5:1 to AC) presence in dialyzed C-Dots and thermally treated at 250°C dialyzed C-Dots in figure 3.51 has different effect on conjugations. Here modes related to Bismuth Oxide are visible, especially for not thermally treated C-Dots. Also peaks related to C-Dots modes are modified, probably due to inhibition of the PEG-4000 saturated ν_{C-H} modes.

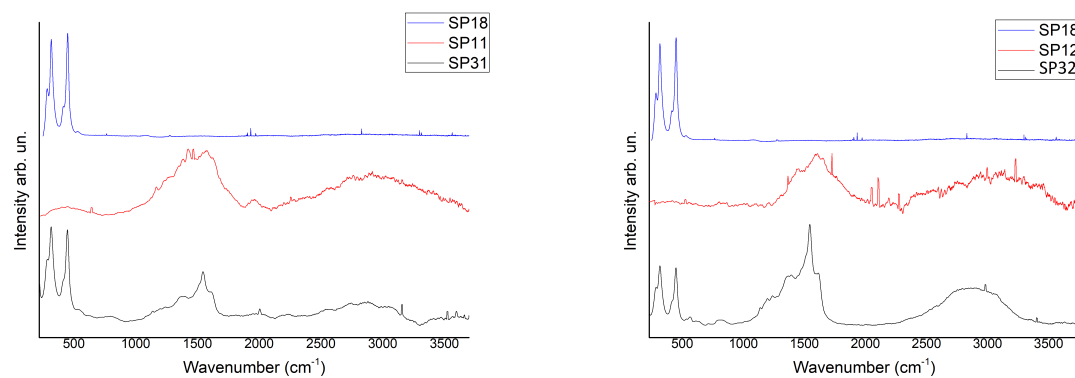


Figure 3.51: Raman spectra of SP31 (left) and SP32 (right) conjugation residue, their C-dots and Bismuth Oxide microparticles

Solid state synthesized Bismuth Oxide based particles conjugated with thermally treated at 250°C with PEG-4000 (0.5:1 to AC) dialyzed C-Dots shown in figure 3.52 (left) presents the same characteristics of that conjugated with several thermally treated C-Dots. The only appreciable difference is a presence of the Bismuth Nitrate characteristic peak approximately at 1050 cm^{-1} , due to the heterogeneity of these microparticles containing both Bi_2O_3 and $\text{Bi}_5\text{O}_7\text{NO}_3$. Instead, for direct conjugation in figure 3.52 (right) the Bismuth Oxide peaks can be observed, so the coverage layer is remarkably thinner than the previous one, considering also the green color of the final product. There are also modes approximately at 1600 cm^{-1} probably due to the C-Dots aromatic structures containing bands D and G.

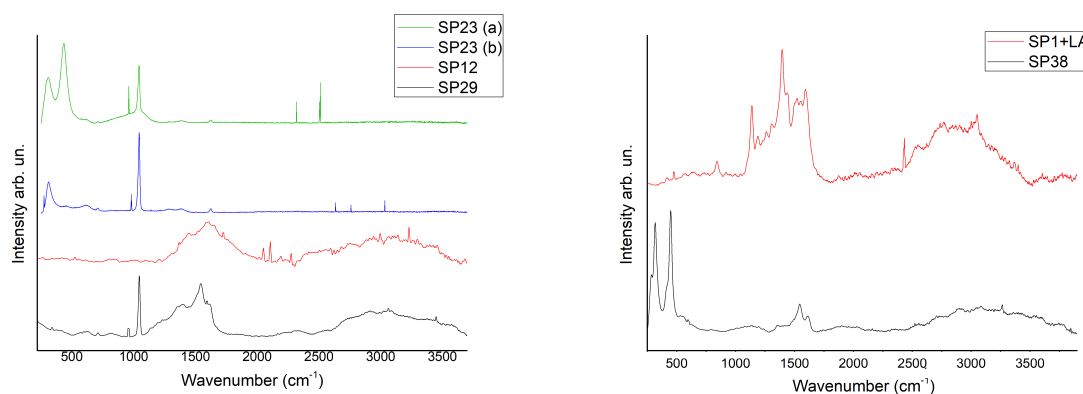


Figure 3.52: Raman spectra of SP29 (left) and SP38 (right) conjugation residue, their C-dots and Bismuth Oxide microparticles

Samples which show a good performance were analyzed also through UV/VIS absorption and photoluminescence spectroscopy and the results are discussed below.

3.3.4 Absorbance UV/VIS

All analyzed conjugation absorption spectra are reported in following figures (3.53, 3.54, 3.55 and 3.56) result difficult to interpret. However, it is possible to think that they arouse from the nature of interaction, involving C-Dots π bonds. In this way the transition states change as a function of number and type of interaction sites.

Figure 3.53 and figure 3.54 report results for conjugation with the thermally treated C-Dots:

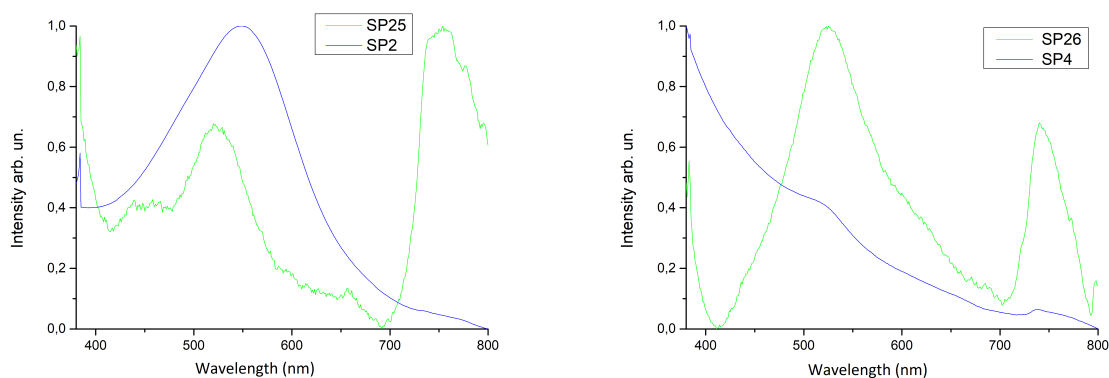


Figure 3.53: Absorption UV/VIS spectrum of SP25 conjugation and its SP2 C-Dots (left) and SP26 conjugation and its SP4 C-Dots (right).

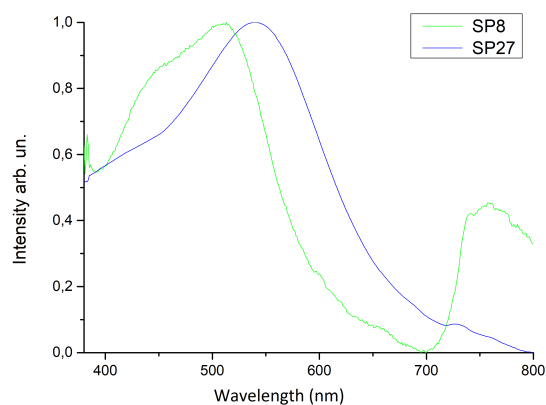


Figure 3.54: Absorption UV/VIS spectrum of SP27 conjugation and its SP8 C-Dots.

Figure 3.55, figure 3.56 report results for conjugation with the dialyzed C-Dots:

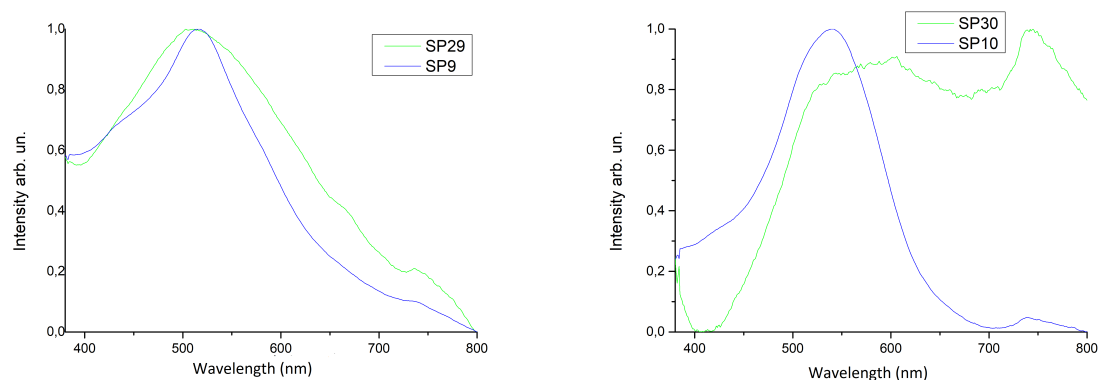


Figure 3.55: Absorption UV/VIS spectrum of SP29 conjugation and its SP9 C-Dots (left) and SP30 conjugation and its SP10 C-Dots (right).

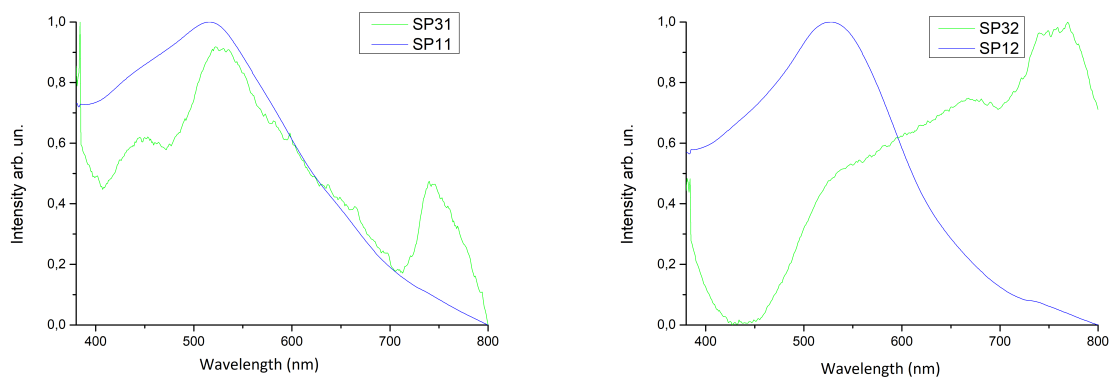


Figure 3.56: Absorption UV/VIS spectrum of SP31 conjugation and its SP11 C-Dots (left) and SP32 conjugation and its SP12 C-Dots (right).

3.3.5 Fluorometer analysis

The most performed conjugation SP33 was also analyzed with fluorometer and the result is reported in figure 3.57:

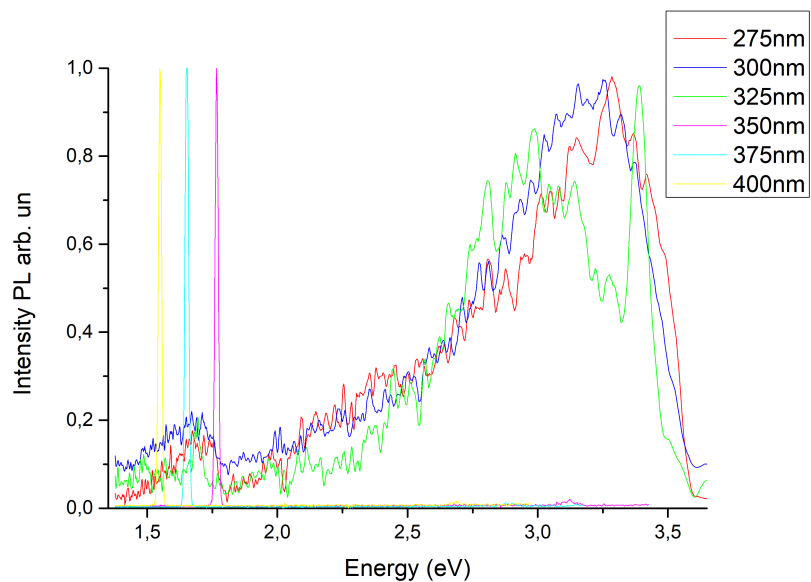


Figure 3.57: Photoluminescent spectra of SP33 which conjugates dialyzed C-Dots and hydrothermal Bismuth Oxide microparticles with PEG-4000 5%.

Differently to the absorption case, the emission spectrum of conjugation is quite similar to that of used C-Dots (figure??), as expected from high photoluminescence of C-Dots.

CHAPTER 4

Conclusions

The bottom-up approach has been used for the C-Dots synthesis, which implies their formation starting from the precursors. The precursors in this work are DPA and CA. Initially they are polymerized and then nucleated. In the first step DPA and AC are placed in the aqueous solution and sonicated promoting in this way the aromatic heterocyclization. One of the possible reactions is obtained by the initial formation of the derivative of amide from AC and DPA reaction and its subsequent transformation in the random cross-linked polymer structure. Another possibility is that the amino groups can react with two carboxyl groups of AC molecule forming an heterocyclic structure and so on. The second step, that is the carbonization, can be carried out by heat treatment and/or purification. On one side, the previously obtained precursor is heated to 250°C, 350°C and 450°C for 10 min. in this way the C-Dots condense and nucleation occurs. Subsequently they were dissolved in deionized (DI) water for 15 min in a ultrasonic bath in order to promote their dissolution and break any aggregations. To purify C-Dots, the solution thus obtained was centrifuged at 10000 rpm for 15 minutes. Only the solubilized part was taken and oven dried, instead the residue was removed away. In this way, only the soluble C-Dots were preserved. Comparing now C-Dots thermally treated at different temperature, it can be deduced that increasing the temperature the C-Dots structure becomes more and more aromatic, as could be seen from the from the band of $\nu_{C=C}$ at 1600cm^{-1} and that of unsaturated ν_{C-H} at 3000cm^{-1} , characteristic of the aromatic structures. This result was expected because due to the thermal treatment the C-Dots condense and carbonization/nucleation takes place. On the other hand, the purification is performed by dialysis, explained though the concept of osmosis. Thanks to the pressure gradient established between the inside and the outside of the membrane the precursor is purified, proportionally to the membrane cutoff (4000 g/mol molecular mass cutoff were used), from the too small organic molecules and oligomers which didn't polymerize in the previous step. The previously obtained C-Dots precursor was put inside the dialysis membrane and agitated. It can be hypothesized that in both cases the C-Dots are composed by sp^2 and sp^3 hybridized carbon structures with size of few nanometers and present a random cross-linked polymer structures which are organized in parallel

planes with external functional groups are obtained and. Comparing the two purification methods it arises that the heat treatment results in a more heterogeneous and disordered structure with many external functional groups, instead the dialyzed one has more compact structure, less flexible with an intense of C=C and C-H bonds, respectively at 1600cm^{-1} and 3000cm^{-1} , typical of the aromatic rings. So, it is possible to choose the method to use basing on the properties one wants to get. Another set of C-Dots synthesis was repeated including PEG-4000 as a non-ionic reagent and adding it in 1:1, 0.5:1 and 0.1:1 proportions with respect to Citric Acid and subsequently treated at 250°C and purified by the centrifugation or directly by means of dialysis membrane. In this case PEG acts as a separator which avoids the C-Dots aggregation, promotes the aromatic compounds condensation and, reacting with their functional groups, maximizes the subsequent conjugation. Indeed, it is observed from obtained spectrums that increasing PEG concentration enhances the $\nu_{\text{C}=\text{C}}$ (1600cm^{-1}) of the aromatic ring. Also the peak of the saturated $\nu_{\text{C}-\text{H}}$ (3000cm^{-1}) is increased due to its presence in PEG. From the Raman spectrum it can be observed that the C-Dots synthesized in these ways present a high number of well defined peaks, but are very fluorescent due to the presence of their functional groups. So even though the low intensity laser (green light 514 nm was used) is used the ratio signal/noise remains low covering a part of the bands, therefore the presence of D and G bands common to all samples can be only supposed. Fluorometer was implemented to take certainty of their photoluminescent features. Also absorption spectra were studied. For the hydrothermal synthesis of the Bismuth Oxide particles, $\text{Bi}(\text{NO}_3)_3 \times 5\text{H}_2\text{O}$ and HNO_3 are used as precursors. The solution is made in an acidic environment in order to promote the $\text{Bi}(\text{NO}_3)_3$ solubility, which is poorly soluble in water. Then a base, sodium hydroxide, is added at room temperature, because this reaction is exothermic, forming bismuth hydroxide which is extremely unstable. The synthesis is stirred and heated at 80° for 3h forming the precipitate of Bismuth Oxide, which is recovered by filtering. This synthesis is repeated adding four different active surfactants (PEG-4000, SLS, LA and PVP) in order to test their ability to direct the planes growth of the synthesis, thanks to their hydrophilic and hydrophobic, and avoid the aggregation between microparticles. From FESEM images, the particles of Bismuth Oxide without active surfactants show the irregular structures, there are breaks due to the planes that grow into a castle of paper and collapse. The planes growth is complicated and there is not preferential morphology and direction. Indeed active surfactants, thanks to their hydrophilic and hydrophobic, orient and aggregate the triangular planes either parallel one to each other or intertwined. The more regular growth was obtained adding PEG and SLS as active surfactants, the structures are organized in tetrahedral shape. The situation is different for PVP and LA. Their morphology is irregular, disordered and without preferential planes of growth. LA contains different geometrical shapes inside its sample. This can be explained by the fact that maybe these active surfactants have not dissolved and consequently they have not performed their function. Analyzing Raman spectrums of these microparticles, it is evident that the characteristic peak of $\text{Bi}(\text{NO}_3)_3$ (1050cm^{-1})

disappears, suggesting that the reaction is occurred completely. Also the peaks of Bismuth Oxide (below 500cm^{-1}), denoting the ν_{B-O} in different proportions due to different active surfactants, are well evident. Furthermore, it is observed that for PVP the structure is grown bad and it is strongly defected. Also the solid state syntheses are performed starting from Bismuth Nitrate pentahydrate without solvent. Thermal decomposition of bismuth is carried out using different calcination temperatures in a gradual way (200°C for 1h, 300°C for 2h, 425°C for 2h) obtaining the heterostructures containing Bi_2O_3 and $\text{Bi}_5\text{O}_7(\text{NO})_3$. Their Raman spectrum still contains the typical Bismuth Nitrate peak, so the conversion in Bismuth Oxide is only partial. Analyzing the same sample in different points, it is evident that the peaks are not all the same because this is an intermediate level, where the structure is extremely heterogeneous. Conjugation the solid state synthesized particles are stirred up with different types of purified C-Dots for 48h. Subsequently the product is centrifuged in order to separate the soluble part, containing C-Dots which have not conjugate, and residue, which is logical that contains the Bismuth Oxide particles conjugated with C-Dots through the weak interactions of H-bond with hydroxyl functions and between the π orbitals of the C-Dots, due to their aromatic structure, and d orbitals present on the microparticles surfaces. The interaction with molecules of Bismuth Oxide stiffens the structure and changes the vibrational modes of the C-Dots, as is seen from their IR spectrums. The band due to unsaturated ν_{C-H} (3000cm^{-1}) is inhibited due to the $\pi - d$ interaction with the particles' surface. Also $\nu_{C=C}$ (1600cm^{-1}) band decreases in intensity because the ring vibration is inhibited due to these interactions. The Raman spectrum reminds to that of C-Dots, but in this case it is difficult to appreciate differences in peaks due to strongly noised C-Dots Raman signal. Due to the fact that there no any characteristic peak of Bismuth Oxide or Bismuth Nitrate, it can be deduced that the C-Dots coverage layer is quite thick. Same syntheses were repeated for hydrothermally synthesized microparticles containing PEG-4000, since they demonstrate the best structural morphology. The microparticles synthesized with this active surfactant present a most regular tetrahedral morphology. Also in these cases IR and Raman spectroscopy confirm the conjugation between Bismuth Oxide microparticles and C-Dots. Differently to the solid state particles, in this case some Raman spectra present also peaks related to Bismuth Oxide, due to different vibration modes Bi-O aroused from interaction.

The direct synthesis of microparticles and their conjugation with C-Dots is made by repeating all steps of the hydrothermal synthesis but adding also C-Dots after the Bismuth Hydroxide formation. Also here the inhibition of $\nu_{C=C}$ (1600cm^{-1}) and unsaturated ν_{C-H} (3000cm^{-1}) band is observed by IR inspection. From Raman spectrum the Bismuth Oxide peaks can be observed, but there are also bands probably due to the C-Dots aromatic structures containing bands D and G.

FESEM images of conjugation containing dialyzed C-Dots and hydrothermally synthesized microparticles reveal the exfoliation of Bismuth Oxide planes as a consequence of conjugation. C-Dots absorption and emission bands were

produced and investigated, due to their excellent optical properties. All these aspect are confirmed with some experiments presented in literature . All the results of this project have been satisfactory and they stimulate improvement of the synthesis methods and investigation of the nanoparticles core structure and properties.

CHAPTER 5

Acknowledgements

First of all, I would like to express my gratitude to my supervisor professor Alberto Tagliaferro, who assisted and guided me throughout this project. Thank you for giving me this opportunity to be a part of your research group, it was a great experience.

I am deeply grateful to dr. Mattia Bartoli for his assistance at every stage of my project, insightful comments and suggestions. Thank you for your patience and availability even on Sunday, I really appreciate it.

I would like to extend my sincere thanks to Andrea, Cristian, Filippo and Giovanni for having shared, for better or for worse, these months in laboratory with me.

I would also like to thank my beloved mother and Giovanni, whom without this would have not been possible. Thank you for your continuous support and understanding.

My heartfelt thanks to Vincenzo, my better half, for your understanding, your never-ending encouragement, unconditional love and for always being there for me. I am happy to have you by my side and share many experiences with you

Special thanks go to Martina infinite friendship, understanding, support and having shared so many experiences together.

Thanks should also go to Viktoriia, even if you are far away I know that I can always count on you.

Thanks to Giordano, to love me as a sister. I always remember with a smile the moments spent together.

I wish to extend my special thanks to Anna Chiara, Marta and Nicoletta, who can always make me smile.

Thanks to Marta, a good friend rather than roommate, I have always appreciated your presence and support.

Heartfelt thanks go to my roommates Agata, Alessandra, Giada e Manuela for your support, good words when I needed them. Thank you above all for having endured my endless and annoying alarm clocks in this last period.

Thanks to all the people who have been close to me over the years: Alessio, Andrea, Linda, Rebecca e Simone. You are always in my heart.

CHAPTER 6

Bibliography

1. Poole Jr, Charles P., and Frank J. Owens. Introduction to nanotechnology. John Wiley & Sons, 2003.
2. Emerich, Dwaine F., and Christopher G. Thanos. "Nanotechnology and medicine." *Expert opinion on biological therapy* 3.4 (2003): 655-663.
3. Jeelani, S., et al. "Theranostics: A treasured tailor for tomorrow." *Journal of pharmacy bioallied sciences* 6.Suppl 1 (2014): S6.
4. Xie, Jin, Seulki Lee, and Xiaoyuan Chen. "Nanoparticle-based theranostic agents." *Advanced drug delivery reviews* 62.11 (2010): 1064-1079.
5. Zulkifli, Z. A., et al. "Synthesis and characterisation of bismuth oxide nanoparticles using hydrothermal method: the effect of reactant concentrations and application in radiotherapy." *Journal of Physics: Conference Series*. Vol. 1082. No. 1. IOP Publishing, 2018.
6. Alqathami, Mamdooh, et al. "Enhancement of radiation effects by bismuth oxide nanoparticles for kilovoltage x-ray beams: a dosimetric study using a novel multi-compartment 3D radiochromic dosimeter." *Journal of Physics: Conference Series*. Vol. 444. No. 1. IOP Publishing, 2013.
7. Mewada, Ashmi, et al. "Swarming carbon dots for folic acid mediated delivery of doxorubicin and biological imaging." *Journal of Materials Chemistry B* 2.6 (2014): 698-705.
8. Mazrad, Zihnil Adha Islamy, et al. "Temperature-sensitive carbon dots derived from poly (N-isopropylacrylamide) for fluorescence on-off properties." *Rsc Advances* 7.18 (2017): 11149-11157.
9. Xu, Xiaoyou, et al. "Electrophoretic analysis and purification of fluorescent single-walled carbon nanotube fragments." *Journal of the American Chemical Society* 126.40 (2004): 12736-12737.
10. Lim, Shi Ying, Wei Shen, and Zhiqiang Gao. "Carbon quantum dots and their applications." *Chemical Society Reviews* 44.1 (2015): 362-381.
11. Mintz, Keenan J., Yiqun Zhou, and Roger M. Leblanc. "Recent development of carbon quantum dots regarding their optical properties, photoluminescence mechanism, and core structure." *Nanoscale* 11.11 (2019): 4634-4652.
12. Siddique, Abu Bakar, et al. "Amorphous carbon dots and their remarkable ability to detect 2, 4, 6-trinitrophenol." *Scientific reports* 8.1 (2018): 1-10.

13. Ansi, V. A., and N. K. Renuka. "Exfoliated graphitic carbon dots: application in heavy metal ion sensing." *Journal of Luminescence* 205 (2019): 467-474.
14. Martindale, Benjamin CM, et al. "Enhancing light absorption and charge transfer efficiency in carbon dots through graphitization and core nitrogen doping." *Angewandte Chemie* 129.23 (2017): 6559-6563.
15. Kelarakis, Antonios. "From highly graphitic to amorphous carbon dots: A critical review." *MRS Energy Sustainability* 1 (2014).
16. Sun, Ya-Ping, et al. "Quantum-sized carbon dots for bright and colorful photoluminescence." *Journal of the American Chemical Society* 128.24 (2006): 7756-7757.
17. Li, Yan, et al. "Nitrogen-doped graphene quantum dots with oxygen-rich functional groups." *Journal of the American Chemical Society* 134.1 (2012): 15-18.
18. Miao, Shihai, et al. "Hetero-atom-doped carbon dots: Doping strategies, properties and applications." *Nano Today* 33 (2020): 100879.
19. Zhou, Yiqun, et al. "Polymers in carbon dots: a review." *Polymers* 9.2 (2017): 67.
20. Zhu, Shoujun, et al. "The photoluminescence mechanism in carbon dots (graphene quantum dots, carbon nanodots, and polymer dots): current state and future perspective." *Nano research* 8.2 (2015): 355-381.
21. Koutsogiannis, Panagiotis, et al. "Advances in fluorescent carbon dots for biomedical applications." *Advances in Physics: X* 5.1 (2020): 1758592.
22. Mintz, Keenan J., et al. "A deep investigation into the structure of carbon dots." *Carbon* 173 (2021): 433-447.
23. Pan, Dengyu, et al. "Hydrothermal route for cutting graphene sheets into blue-luminescent graphene quantum dots." *Advanced materials* 22.6 (2010): 734-738.
24. Dong, Yongqiang, et al. "Blue luminescent graphene quantum dots and graphene oxide prepared by tuning the carbonization degree of citric acid." *Carbon* 50.12 (2012): 4738-4743.
25. Tang, Libin, et al. "Deep ultraviolet photoluminescence of water-soluble self-passivated graphene quantum dots." *ACS nano* 6.6 (2012): 5102-5110.
26. Liu, Meng Li, et al. "Carbon dots: synthesis, formation mechanism, fluorescence origin and sensing applications." *Green chemistry* 21.3 (2019): 449-471.
27. Ma, Zhuoran, et al. "Deep learning for in vivo near-infrared imaging." *Proceedings of the National Academy of Sciences* 118.1 (2021).
28. Liyanage, Piumi Y., et al. "Carbon nitride dots: a selective bioimaging nanomaterial." *Bioconjugate chemistry* 30.1 (2018): 111-123.
29. Liyanage, Piumi Y., et al. "Pediatric glioblastoma target-specific efficient delivery of gemcitabine across the blood-brain barrier via carbon nitride dots." *Nanoscale* 12.14 (2020): 7927-7938.
30. Xiong, Yuan, et al. "Influence of molecular fluorophores on the research field of chemically synthesized carbon dots." *Nano Today* 23 (2018): 124-139.
31. Sarkar, Sunandan, et al. "Graphitic nitrogen doping in carbon dots causes red-shifted absorption." *The Journal of Physical Chemistry C* 120.2 (2016): 1303-1308.

-
32. Hola, Katerina, et al. "Graphitic nitrogen triggers red fluorescence in carbon dots." *ACS nano* 11.12 (2017): 12402-12410.
 33. Bao, Lei, et al. "Electrochemical tuning of luminescent carbon nanodots: from preparation to luminescence mechanism." *Advanced materials* 23.48 (2011): 5801-5806.
 34. Xia, Chenghui, et al. "Size-dependent band-gap and molar absorption coefficients of colloidal CuInS₂ quantum dots." *ACS nano* 12.8 (2018): 8350-8361.
 35. Liu, Mengli. "Optical properties of carbon dots: a review." *Nanoarchitectonics* (2020): 1-12.
 36. Hu, Shengliang, et al. "Tunable photoluminescence across the entire visible spectrum from carbon dots excited by white light." *Angewandte Chemie International Edition* 54.10 (2015): 2970-2974.
 37. Zhang, Yijun, et al. "Multicolour nitrogen-doped carbon dots: tunable photoluminescence and sandwich fluorescent glass-based light-emitting diodes." *Nanoscale* 9.45 (2017): 17849-17858.
 38. Kim, Sung, et al. "Anomalous behaviors of visible luminescence from graphene quantum dots: interplay between size and shape." *ACS nano* 6.9 (2012): 8203-8208.
 39. Shen, Jianhua, et al. "Facile preparation and upconversion luminescence of graphene quantum dots." *Chemical communications* 47.9 (2011): 2580-2582.
 40. Yan, Fanyong, et al. "The fluorescence mechanism of carbon dots, and methods for tuning their emission color: a review." *Microchimica Acta* 186.8 (2019): 1-37.
 41. Hu, Chao, et al. "Design and fabrication of carbon dots for energy conversion and storage." *Chemical Society Reviews* 48.8 (2019): 2315-2337.
 42. Xia, Chenghui, et al. "Size-dependent band-gap and molar absorption coefficients of colloidal CuInS₂ quantum dots." *ACS nano* 12.8 (2018): 8350-8361.
 43. Gan, Zhixing, et al. "Is there real upconversion photoluminescence from graphene quantum dots?" *Advanced Optical Materials* 1.8 (2013): 554-558.
 44. Ma, Zhuoran, et al. "Deep learning for in vivo near-infrared imaging." *Proceedings of the National Academy of Sciences* 118.1 (2021).
 45. Rana, Anu, Krishna Yadav, and Sheeja Jagadevan. "A comprehensive review on green synthesis of nature-inspired metal nanoparticles: Mechanism, application and toxicity." *Journal of Cleaner Production* (2020): 122880.
 46. Wang, Yanli, et al. "Toxic effects of metal oxide nanoparticles and their underlying mechanisms." *Science China Materials* 60.2 (2017): 93-108.
 47. Li, Qin, et al. "Photoluminescent carbon dots as biocompatible nanoprobes for targeting cancer cells in vitro." *The Journal of Physical Chemistry C* 114.28 (2010): 12062-12068.
 48. Nurunnabi, Md, et al. "In vivo biodistribution and toxicology of carboxylated graphene quantum dots." *ACS nano* 7.8 (2013): 6858-6867.
 49. Tao, Huiquan, et al. "In vivo NIR fluorescence imaging, biodistribution, and toxicology of photoluminescent carbon dots produced from carbon nanotubes and graphite." *Small* 8.2 (2012): 281-290.
 50. Zhu, Shoujun, et al. "Strongly green-photoluminescent graphene quantum

- dots for bioimaging applications." *Chemical communications* 47.24 (2011): 6858-6860.
51. Cao, Li, et al. "Carbon dots for multiphoton bioimaging." *Journal of the American Chemical Society* 129.37 (2007): 11318-11319.
 52. Goh, Eun Ji, et al. "Bioimaging of hyaluronic acid derivatives using nano-sized carbon dots." *Biomacromolecules* 13.8 (2012): 2554-2561.
 53. Kong, Biao, et al. "Carbon dot-based inorganic-organic nanosystem for two-photon imaging and biosensing of pH variation in living cells and tissues." *Advanced materials* 24.43 (2012): 5844-5848.
 54. Liu, Changjun, et al. "Nano-carrier for gene delivery and bioimaging based on carbon dots with PEI-passivation enhanced fluorescence." *Biomaterials* 33.13 (2012): 3604-3613.
 55. Hsu, Pin-Che, et al. "Extremely high inhibition activity of photoluminescent carbon nanodots toward cancer cells." *Journal of Materials Chemistry B* 1.13 (2013): 1774-1781.
 56. Riggs, Jason E., et al. "Strong luminescence of solubilized carbon nanotubes." *Journal of the American Chemical Society* 122.24 (2000): 5879-5880.
 57. Bechet, Denise, et al. "Nanoparticles as vehicles for delivery of photodynamic therapy agents." *Trends in biotechnology* 26.11 (2008): 612-621.
 58. Kleinauskas, Andrius, et al. "Carbon-core silver-shell nanodots as sensitizers for phototherapy and radiotherapy." *Nanotechnology* 24.32 (2013): 325103.
 59. Rani, Reshma, Vinit Kumar, and Flavio Rizzolio. "Fluorescent carbon nanoparticles in medicine for cancer therapy: An update." (2018): 4-5.
 60. Yan, Fanyong, et al. "Highly photoluminescent carbon dots-based fluorescent chemosensors for sensitive and selective detection of mercury ions and application of imaging in living cells." *Sensors and Actuators B: Chemical* 192 (2014): 488-495.
 61. Li, Hailong, et al. "Nucleic acid detection using carbon nanoparticles as a fluorescent sensing platform." *Chemical Communications* 47.3 (2011): 961-963.
 62. Hsu, Pin-Che, et al. "Extremely high inhibition activity of photoluminescent carbon nanodots toward cancer cells." *Journal of Materials Chemistry B* 1.13 (2013): 1774-1781.
 63. Liu, Yong, and Peiyi Wu. "Graphene quantum dot hybrids as efficient metal-free electrocatalyst for the oxygen reduction reaction." *ACS applied materials interfaces* 5.8 (2013): 3362-3369.
 64. Li, Haitao, et al. "Water-soluble fluorescent carbon quantum dots and photocatalyst design." *Angewandte Chemie International Edition* 49.26 (2010): 4430-4434.
 65. Essner, Jeremy B., and Gary A. Baker. "The emerging roles of carbon dots in solar photovoltaics: a critical review." *Environmental Science: Nano* 4.6 (2017): 1216-1263.
 66. Ngo, Yen-Linh Thi, et al. "Electrochemical Biosensors based on Nanocomposites of Carbon-based Dots." *Korean Chemical Engineering Research* 58.4 (2020): 499-513.
 67. Chen, Bin Bin, et al. "A large-scale synthesis of photoluminescent carbon

- quantum dots: a self-exothermic reaction driving the formation of the nanocrystalline core at room temperature." *Green Chemistry* 18.19 (2016): 5127-5132.
68. Buot, F. A., and J. W. McClure. "Theory of diamagnetism of bismuth." *Physical Review B* 6.12 (1972): 4525.
69. Fukuyama, Hidetoshi. "Inter-band effects of magnetic field on orbital susceptibility and Hall conductivity—case of bismuth." *Annalen der Physik* 15.7-8 (2006): 520-525.
70. Mohan, Ram. "Green bismuth." *Nature chemistry* 2.4 (2010): 336-336.
71. Yang, Yang, et al. "Bismuth complexes: synthesis and applications in biomedicine." *Journal of Coordination Chemistry* 68.3 (2015): 379-397.
72. Torrìsi, Lorenzo, et al. "Synthesis of bismuth nanoparticles for biomedical applications." *Atti della Accademia Peloritana dei Pericolanti-Classe di Scienze Fisiche, Matematiche e Naturali* 97.S2 (2019): 12.
73. Caruso, Frank, Taeghwan Hyeon, and Vincent M. Rotello. "Nanomedicine." *Chemical Society Reviews* 41.7 (2012): 2537-2538.
74. Wiederrecht, Gary. *Handbook of nanoscale optics and electronics*. Academic Press, 2010.
75. Azhdarzadeh, Morteza, et al. "Nanotoxicology: advances and pitfalls in research methodology." *Nanomedicine* 10.18 (2015): 2931-2952.
76. Gianfranco, et al. "Synthesis and thermoelectric characterisation of bismuth nanoparticles." *Journal of nanoparticle research* 11.7 (2009): 1729-1738.
77. Carotenuto, Gianfranco, et al. "Synthesis and thermoelectric characterisation of bismuth nanoparticles." *Journal of nanoparticle research* 11.7 (2009): 1729-1738.
78. Shahbazi, Mohammad-Ali, et al. "The versatile biomedical applications of bismuth-based nanoparticles and composites: therapeutic, diagnostic, biosensing, and regenerative properties." *Chemical Society Reviews* 49.4 (2020): 1253-1321
79. Leontie, L., et al. "Structural and optical characteristics of bismuth oxide thin films." *Surface Science* 507 (2002): 480-485.
80. Zulkifli, Z. A., et al. "Synthesis and characterisation of bismuth oxide nanoparticles using hydrothermal method: the effect of reactant concentrations and application in radiotherapy." *Journal of Physics: Conference Series*. Vol. 1082. No. 1. IOP Publishing, 2018.
81. Mohn, D., et al. "Radio-opaque nanosized bioactive glass for potential root canal application: evaluation of radiopacity, bioactivity and alkaline capacity." *International endodontic journal* 43.3 (2010): 210-217.
82. Bi, Huiting, et al. "Bismuth nanoparticles with "light" property served as a multifunctional probe for X-ray computed tomography and fluorescence imaging." *Chemistry of Materials* 30.10 (2018): 3301-3307.
83. Li, Zhenglin, et al. "Dual-stimuli responsive bismuth nanoraspberries for multimodal imaging and combined cancer therapy." *Nano letters* 18.11 (2018): 6778-6788.
84. Jassim, Abdulkadir MN, et al. "Study the antibacterial effect of bismuth oxide and tellurium nanoparticles." *International Journal of Chemical and Biomolecular Science* 1.3 (2015): 81-84.

-
85. Thomas, F., B. Bialek, and R. Hensel. "Medical use of bismuth: the two sides of the coin." *J Clin Toxicol* 3 (2012): 004.
 86. Deng, Junjie, et al. "Tumor targeted, stealthy and degradable bismuth nanoparticles for enhanced X-ray radiation therapy of breast cancer." *Biomaterials* 154 (2018): 24-33.
 87. Szostak, Krzysztof, et al. "Bismuth oxide nanoparticles in drug delivery systems." *Pharmaceutical Chemistry Journal* 53.1 (2019): 48-51.
 88. Kiil, Fredrik. "Mechanism of osmosis." *Kidney international* 21.2 (1982): 303-308.
 89. Kou, Yan, et al. "Thermal analysis and heat capacity study of polyethylene glycol (PEG) phase change materials for thermal energy storage applications." *The Journal of Chemical Thermodynamics* 128 (2019): 259-274.
 90. Ferrari, Andrea C. "Raman spectroscopy of graphene and graphite: Disorder, electron-phonon coupling, doping and nonadiabatic effects." *Solid state communications* 143.1-2 (2007): 47-57.
 91. Sato, K., et al. "D-band Raman intensity of graphitic materials as a function of laser energy and crystallite size." *Chemical physics letters* 427.1-3 (2006): 117-121.
 92. Wang, Yi, and Yunling Li. "Metastable -Bi₂O₃ tetrahedra: Phase-transition dominated by polyethylene glycol, photoluminescence and implications for internal structure by etch." *Journal of colloid and interface science* 454 (2015): 238-244.
 93. Gadhi, Tanveer A., et al. "Insights on the role of -Bi₂O₃/Bi₅O₇NO₃ heterostructures synthesized by a scalable solid-state method for the sunlight-driven photocatalytic degradation of dyes." *Catalysis Today* 321 (2019): 135-145.